NAVAL POSTGRADUATE SCHOOL

MONTEREY, CALIFORNIA

THESIS

SINX/AL METAMATERIAL-BASED TERAHERTZ-TO-INFRARED CONVERTER FOR REAL-TIME IMAGING

by

Sangmin Lee

June 2019

Thesis Advisor: Fabio D. Alves
Co-Advisor: Gamani Karunasiri

THIS PAGE INTENTIONALLY LEFT BLANK

REPORT DOCUMENTATION PAGE			*Form Approved OMB No. 0704-0188*

1. AGENCY USE ONLY *(Leave blank)*	**2. REPORT DATE** June 2019	**3. REPORT TYPE AND DATES COVERED** Master's thesis

4. TITLE AND SUBTITLE SINX/AL METAMATERIAL-BASED TERAHERTZ-TO-INFRARED CONVERTER FOR REAL-TIME IMAGING	**5. FUNDING NUMBERS**
6. AUTHOR(S) Sangmin Lee	
7. PERFORMING ORGANIZATION NAME(S) AND ADDRESS(ES) Naval Postgraduate School Monterey, CA 93943-5000	**8. PERFORMING ORGANIZATION REPORT NUMBER**
9. SPONSORING / MONITORING AGENCY NAME(S) AND ADDRESS(ES) N/A	**10. SPONSORING / MONITORING AGENCY REPORT NUMBER**

11. SUPPLEMENTARY NOTES The views expressed in this thesis are those of the author and do not reflect the official policy or position of the Department of Defense or the U.S. Government.

12a. DISTRIBUTION / AVAILABILITY STATEMENT Approved for public release. Distribution is unlimited.	**12b. DISTRIBUTION CODE** A

13. ABSTRACT (maximum 200 words)

Terahertz (THz) real-time imaging technology can be used in various fields. One way to perform real-time THz imaging is through metamaterial-based MEMS focal plane arrays (FPA). Among different possible configurations, THz-to-IR converters were selected to be studied and developed. The operation principle is using an IR camera to image the heat pattern on the backside of the FPA, generated by the absorption of the THz scene, presented on the front side of the FPA. In this study, we designed and fabricated metamaterials that efficiently absorb 3.8 THz and 4.75 THz, the frequencies of the quantum cascade lasers available in the Naval Postgraduate School Physics Department. Metamaterials that have near 1 emissivity between 20 and 40 THz and near zero elsewhere were also designed. To develop this sensor, the properties of silicon nitride films were investigated using single square unit cells. Next, the geometric configuration of the metamaterial elements were designed using the COMSOL Multiphysics and CST Microwave studio. Finally, the metamaterials were fabricated using tools available in the NPS microfabrication facility (Clean Room). The optimized metamaterial films obtained during thesis work will be used in an optimized THz-to-IR converter to be integrated to a long-wave infrared camera in order to provide a complete THz imaging system.

14. SUBJECT TERMS THz, terahertz, IR, imaging, metamaterial, converter, real-time	**15. NUMBER OF PAGES** 63
	16. PRICE CODE

17. SECURITY CLASSIFICATION OF REPORT	**18. SECURITY CLASSIFICATION OF THIS PAGE**	**19. SECURITY CLASSIFICATION OF ABSTRACT**	**20. LIMITATION OF ABSTRACT**
Unclassified	Unclassified	Unclassified	UU

NSN 7540-01-280-5500 Standard Form 298 (Rev. 2-89) Prescribed by ANSI Std. 239-18

THIS PAGE INTENTIONALLY LEFT BLANK

Approved for public release. Distribution is unlimited.

SINX/AL METAMATERIAL-BASED TERAHERTZ-TO-INFRARED CONVERTER FOR REAL-TIME IMAGING

Sangmin Lee
Lieutenant Commander, Republic of Korea Navy
Bachelor of Science, Republic of Korea Naval Academy, 2007

Submitted in partial fulfillment of the
requirements for the degree of

MASTER OF SCIENCE IN APPLIED PHYSICS

from the

NAVAL POSTGRADUATE SCHOOL
June 2019

Approved by: Fabio D. Alves
Advisor

Gamani Karunasiri
Co-Advisor

Kevin B. Smith
Chair, Department of Physics

THIS PAGE INTENTIONALLY LEFT BLANK

ABSTRACT

Terahertz (THz) real-time imaging technology can be used in various fields. One way to perform real-time THz imaging is through metamaterial-based MEMS focal plane arrays (FPA). Among different possible configurations, THz-to-IR converters were selected to be studied and developed. The operation principle is using an IR camera to image the heat pattern on the backside of the FPA, generated by the absorption of the THz scene, presented on the front side of the FPA. In this study, we designed and fabricated metamaterials that efficiently absorb 3.8 THz and 4.75 THz, the frequencies of the quantum cascade lasers available in the Naval Postgraduate School Physics Department. Metamaterials that have near 1 emissivity between 20 and 40 THz and near zero elsewhere were also designed. To develop this sensor, the properties of silicon nitride films were investigated using single square unit cells. Next, the geometric configuration of the metamaterial elements were designed using the COMSOL Multiphysics and CST Microwave studio. Finally, the metamaterials were fabricated using tools available in the NPS microfabrication facility (Clean Room). The optimized metamaterial films obtained during thesis work will be used in an optimized THz-to-IR converter to be integrated to a long-wave infrared camera in order to provide a complete THz imaging system.

THIS PAGE INTENTIONALLY LEFT BLANK

TABLE OF CONTENTS

THIS PAGE INTENTIONALLY LEFT BLANK

LIST OF FIGURES

LIST OF TABLES

THIS PAGE INTENTIONALLY LEFT BLANK

LIST OF ACRONYMS AND ABBREVIATIONS

Al	Aluminum
Ar	Argon
FPA	Focal Plane Array
FTIR	Fourier Transform Infrared Spectrometer
IR	Infrared
ITU	International Telecommunication Union
MEMS	Microelectromechanical Systems
NPS	Naval Postgraduate School
QCL	Quantum Cascade Laser
ROKN	Republic of Korea Navy
SiN_x	Silicon nitride
SRL	Sensor Research Laboratory
THz	Terahertz
PECVD	Plasma enhanced chemical vapor deposition

THIS PAGE INTENTIONALLY LEFT BLANK

ACKNOWLEDGMENTS

First, I would like to offer a sincere thanks to the Republic of Korea Navy for giving me the chance to study in the Naval Postgraduate School. Most parts of life here were challenging, but it also was an experience with many rewards for me and my family. I would like to thank all the faculty at NPS. I especially will never forget Professors Fabio Alves and Gamani Karunasiri for their mentorship and support. Without their effort, my thesis work would not have gone well. Finally, I want to express my gratitude to my family. I would not do well without my wife's dedication and support of me. In addition, I am grateful that my children did well during these new circumstances without any problems. These gifts allowed me to focus on my work. Also, I would like to thank Joshua Faucett for serving as a sponsor for me and my family. We will never forget you, and your family's friendship and kindness.

THIS PAGE INTENTIONALLY LEFT BLANK

I. INTRODUCTION

Frequencies of electromagnetic radiation have been used for a variety of purposes in modern society. Figure 1 shows that each different frequency of electromagnetic radiation is employed in a diverse range of fields, including radio communication, radar, optical communication, medical, and imaging. Particularly interesting is the terahertz (THz) section of the spectrum due to its special properties. It can penetrate dielectric materials and fabrics, allows for better resolution than millimetric or microwaves, and consists of non-ionizing radiation. The THz imaging technology can be used for security, non-destructive inspection, healthcare, remote sensing, and a variety of other uses.

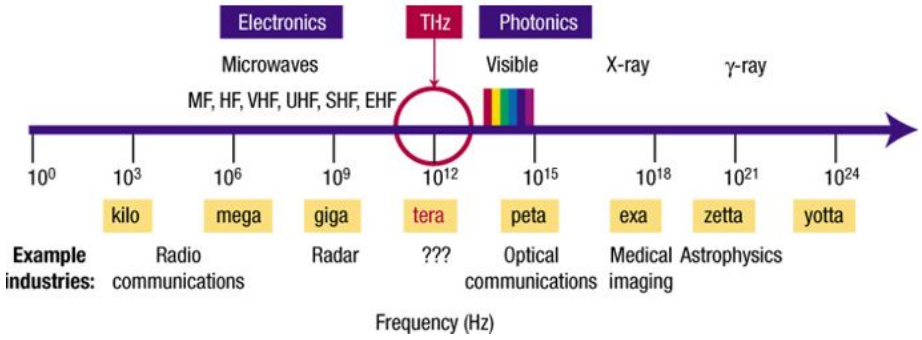

Figure 1. The electromagnetic spectrum. Source: [1].

THz imaging technology can be useful for applications in defense. The first purpose is useful in terms of security. As the troops increase the number of bases opening to the public, the threat of terrorism is also increasing. A thorough security screening is a good way to reduce the threat of terrorism. As seen in Figure 2, THz sensors can detect a gun that is hidden in clothing, with high resolution images. If the military uses the THz imaging technology for security screening, they can prevent attacks from terrorists. Secondly, the military can also use the THz imaging technology for non-destructive inspection. Advantages of non-destructive inspection are safety assurance and increased effectiveness. Diagnosing the accurate cause of equipment failure not only reduces cost, but also improves working efficiency. In the case of a navy ship's equipment failing during an

operation, for example, it will be possible to increase the efficiency of the operation by repairing the ship with an accurate and prompt diagnosis. All the merits of using THz imaging technology are attractive to the Republic of Korea Navy (ROKN).

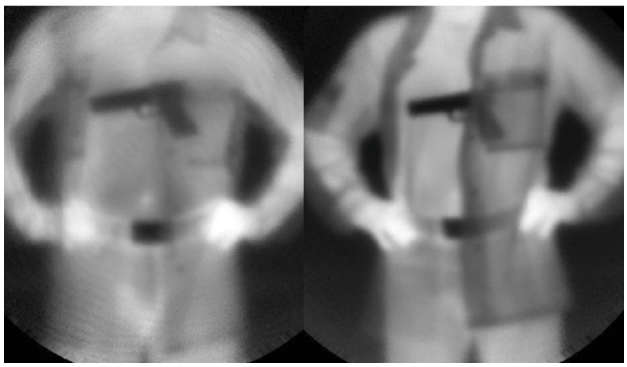

Figure 2. Security screening using THz sensor. Source: [2].

The Sensor Research Laboratory (SRL) at the Naval Postgraduate School (NPS) has been studying the means to realize a real-time THz imager. One attractive way to accomplish this is through the use of metamaterial-based MEMS THz-to-Infrared (IR) converter focal plane arrays (FPA) [3]. A schematic representation of the operation principle of such an imaging scheme is shown in Figure 3. It uses an infrared camera to image the heat pattern on the backside of the focal plane array, generated by the absorption of the THz scene, presented on the front side of the FPA. Due to the low photon energy at THz frequencies, imaging at room temperature is performed using an illumination source. Quantum cascade lasers (QCL) are typically used for frequencies between 1 and 10 THz due to their compactness and power throughput. On the other end, an uncooled long-wave infrared (LWIR) camera is used for simplicity. The sensor consists of metamaterial films optimized to absorb heat from objects in the THz range of interest, and emits a readout on the band of the infrared camera. In this study we design a series of planar metamaterials that can efficiently absorb 3.8 THz and 4.75 THz, the frequencies of the QCLs available in the NPS Physics Department, and selectively emit in the LWIR or have the outward infrared flux between 20 and 40 THz. The planar metamaterials (meta surfaces) configuration used in this work is comprised of a periodic repetition of metallic elements

(resonator) separated from a homogeneous metallic layer (ground plane) by a dielectric spacer. While the functionality of the metallic layer is only related to the optical properties, the dielectric layer is also used in the structure of the sensor (pixel). Alves et al. [4] demonstrated that absorptivity and emissivity can be controlled by a geometric configuration of resonator.

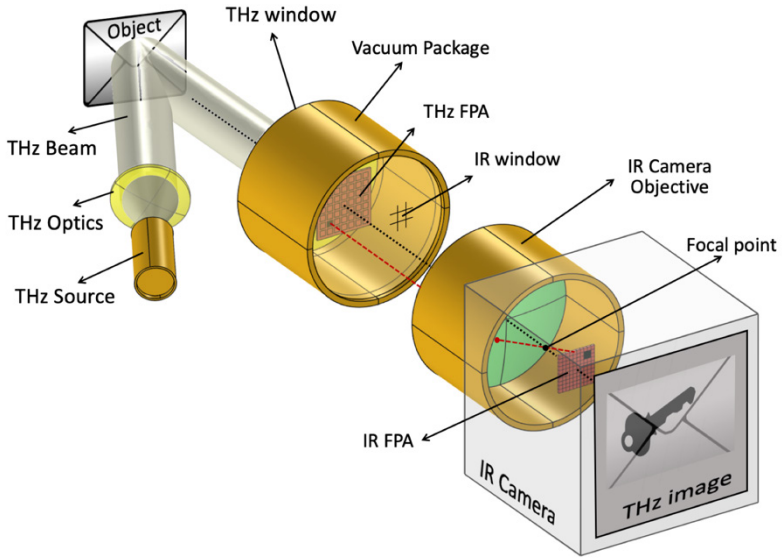

The schematic diagram shows how to work a THz-to-IR converter. The terahertz beam emits to the object that is covered up by the envelope. The THz focal plane array that sits in the vacuum chamber absorbs the refracted beam from the object. The IR focal plane array that sits in the IR camera emits the beam. A commercial IR camera images the heat pattern.

Figure 3. The concept of a THz-to-IR converter for real-time imaging. Source: [3].

Alves et al. [3] also demonstrated the concepts of a THz-to-IR converter based on planar metamaterials using aluminum (Al) with silicon dioxide (SiO_x). They defined the considered conversion efficiency as the ratio between the changing flux in IR readings within the spectrum band of a commercial IR camera, $\Delta\Phi_{vIR}$, and the total changing incident flux, $\Delta\Phi_0$, and it can be calculated by

$$eff = \frac{\Delta\Phi_{vIR}}{\Delta\Phi_0} = \frac{A_0\pi(\int_{v1}^{v2} \varepsilon_{IR}(v)L_{ov}(T)dv - \int_{v1}^{v2} \varepsilon_{IR}(v)L_{ov}(T_0))dv}{\Delta\Phi_0} \quad (1)$$

where $A_0\pi$ is the sensor surface area, using the concept of solid angle. ε_{IR} is the backside of the IR sensor's emissivity, T_0 is the initial temperature of the sensor, T is the final temperature of the sensor. L_{ov} is the spectral radiance and it is given by

$$L_{ov} = \left(\frac{2hv^3}{c^2}\right) \times \left(\frac{1}{e^{\left(\frac{hv}{kT}\right)-1}}\right) \quad (2)$$

where c is the speed of light in a vacuum, k is Boltzmann's constant, h is Plank's constant, and T is the temperature of the sensor. It can be seen in equations (1) and (2) that to maximize the efficiency of the THz absorber, the response must be as narrow as possible and perfectly matched with the illumination source. The IR emitter should have a blackbody like response within the band of the readout, while remaining near zero elsewhere.

In this context, the main goal of this thesis is to improve conversion efficiency, using Al/silicon nitride (SiN_x)/Al metamaterial structures, and new resonator geometries. To do this, the properties of the SiN_x films grown at the NPS microfabrication facility must be investigated. Next, the construction of the geometric configuration of the resonator elements should be studied, using COMSOL Multiphysics and the CST Microwave Studio. Next, optimized metamaterial films for THz absorption and IR emission should be fabricated. The films will be characterized and the results used to refine the computational models. After a few cycles, the optimized metamaterial structures will be used as part of a THz-to-IR converter focal plane array to be fabricated in future work.

II. SILICON NITRIDE REFRACTIVE INDEX

In order to obtain the refractive index of the SiN_x film over a large interval of frequencies, from 1 to 50 THz, a new technique is used. The refractive index is a complex-value that consists of real and imaginary parts related to refraction and attenuation, respectively. In the NPS microfabrication facility, the silicon nitride films are grown using PECVD (Plasma Enhanced Chemical Vapor Deposition) with a mixture of two gases – Argon (Ar) and Silane (SiH_4) at around 10 mTorr. The films obtained by this process are nonstoichiometric (SiN_x) while the concentration of nitrogen influences the refractive index of the material.

In order to obtain the refractive index of SiN_x in a wide spectral range (from IR to THz), the representative characteristic of metamaterial perfect absorbers is used. $Al/SiN_x/Al$ metamaterial films are fabricated to provide a wide range of resonant responses, and then a finite element simulation is performed and the refractive index of SiN_x is altered until a good fit is obtained. The detailed process can be described as a series of design, fabrication, and analysis.

A. DESIGN

Using finite element modeling, the COMSOL Multiphysics and CST Microwave Studio metamaterial structures are simulated. Due to the periodicity of the films, simulations can be performed in a unit-cell basis.

Figure 4 shows a schematic representation of a metamaterial unit cell where the $Al/SiN_x/Al$ cell is sandwiched by air layers, and subsequently further sandwiched by perfect matching layers (PML) that assure there will be no cavitation (no reflection on the external boundaries will reach back to the cell). The lateral boundaries are set as periodic boundaries to account for an infinite repetition of the same cell in all directions. Active and passive ports are inserted in order to read the scattering parameters, which are used to compute the absorptivity and emissivity of the structure. A planar wave is sent from port 1 with the direction perpendicular to the cell. The reflected portion of the wave allows the

computation of $|s_{11}|^2 = \frac{P_{Reflected}}{P_0}$, which represents the reflectivity of the structure. The transmissivity is computed on port 2, $|S_{21}|^2 = \frac{P_{Transmitted}}{P_0}$. All the designed structures of the Al (the metal ground plane shown in Figure 4) are much thicker than the skin depth at the spectral range of interest, $|S_{21}|^2 = 0$. This means that there is no transmission. Because of the size of the representing metallic elements (the resonators) the second order scattering is negligible and absorptivity can be obtained as,

$$A = 1 - |S_{11}|^2 \tag{3}$$

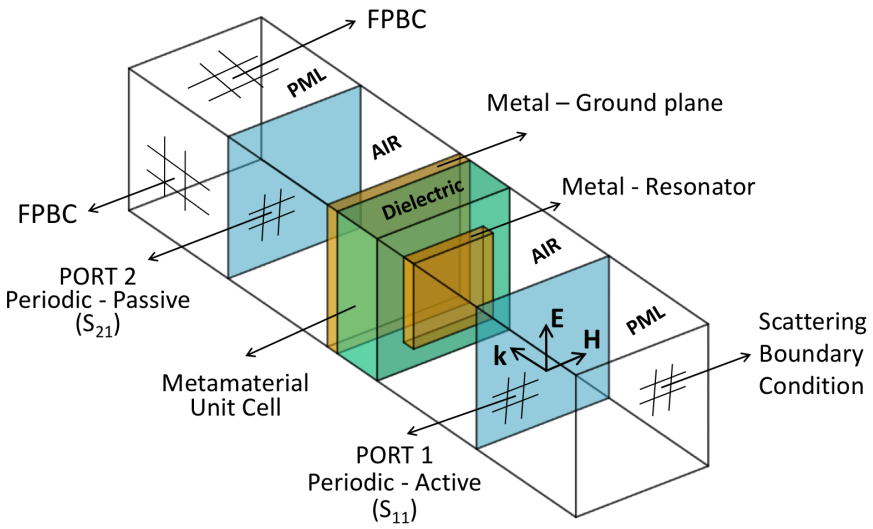

The metamaterial unit cell located between perfectly matched layers (PML). The FPBC is defined as the Floquet Periodic Boundary Condition. Aluminum is used for the ground plane and resonator, and silicon nitride is used for dielectric material.

Figure 4. Schematic diagram concept of the COMSOL simulation. Source: [3].

The material properties used in the simulation (in this phase) were obtained from open source [5] and, therefore, not correspondent to the actual properties of the materials used in the fabrication. Structures comprised of the following unit cells (Table 1) were simulated and resonant responses were found from 3 to 8 THz.

Table 1. Simulated and measured THz absorption of metamaterial structures

	Unit cell	Simulation	Measurement
1	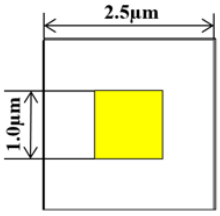	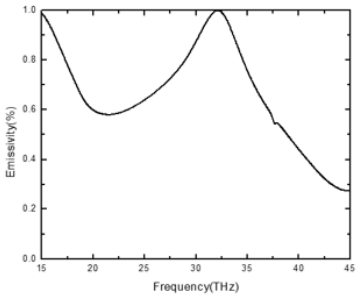	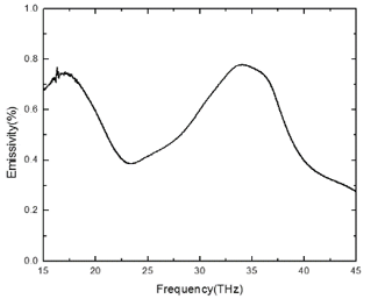
2	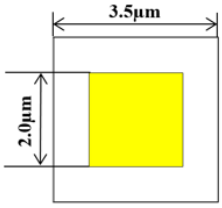	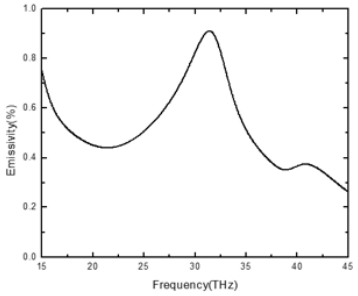	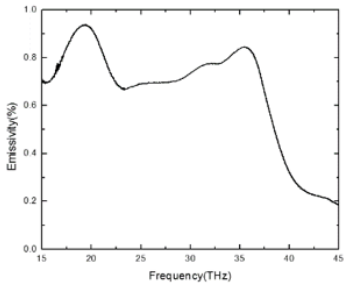
3	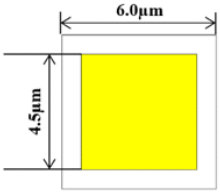	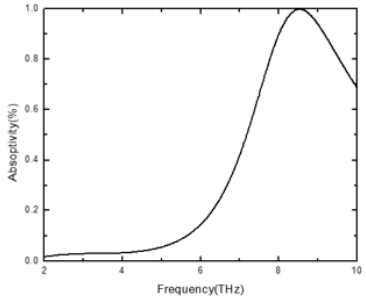	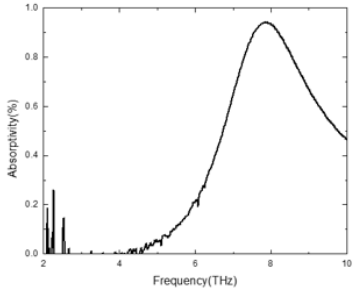

Table cont'd on next page

Table cont'd from previous page

4	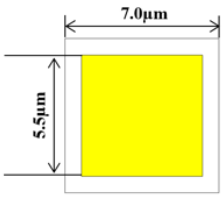	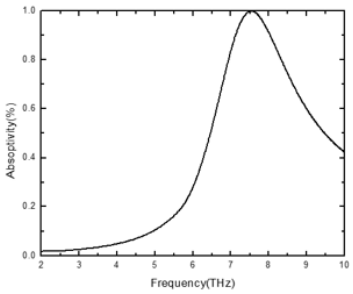	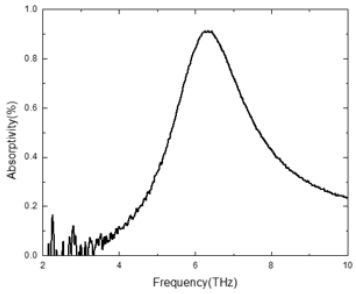
5	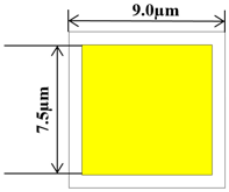	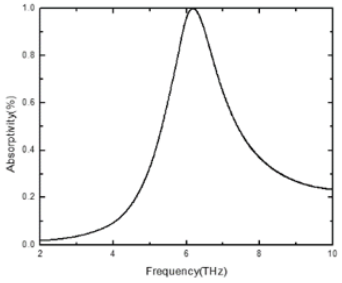	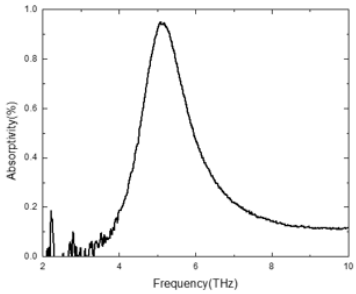
6	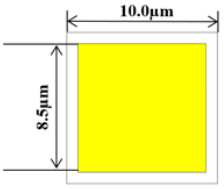	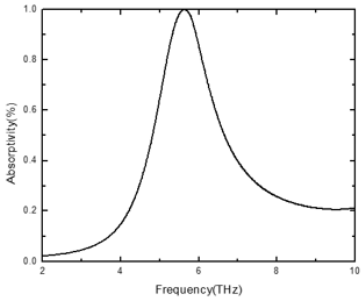	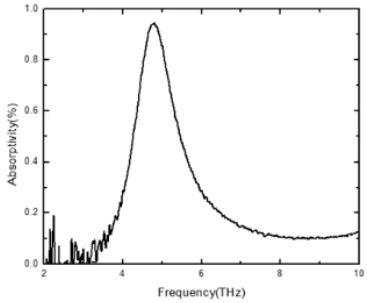

The thickness of the Al layers is 80 nm and the SiNx layer is 1.6 μm. The sizes of the squares were designed from 1 to 10 μm with 0.5 μm intervals. The gap is maintained at 1.5 μm. The metamaterial structures that have 11 μm and 14 μm square with 4 μm gap were simulated and fabricated. The gap can be defined as the distance between squares.

The width of the absorptivity is determined by the imaginary part of the refractive index (extinction coefficient) and the resonance peak is determined by the real part of the refractive index. The thickness of the dielectric layer also influences the absorptivity of the metamaterial. Shifts in resonant peaks as well as changes in the magnitude of response are observed. The thickness of the films will impact the operation of the finely produced

thermal sensor. Thicker films will make slower sensors, therefore a compromise has to be done when selecting the thickness of the SiN_x film.

The designed metamaterial structures were laid out for treatment by a substrate of 4 inches, and the distribution of these structures is shown in Figure 5. The sample was divided into 21 sections. Each section has a different resonator square size. The layout shown in Figure 5 was used to build the photomask used to fabricate the films.

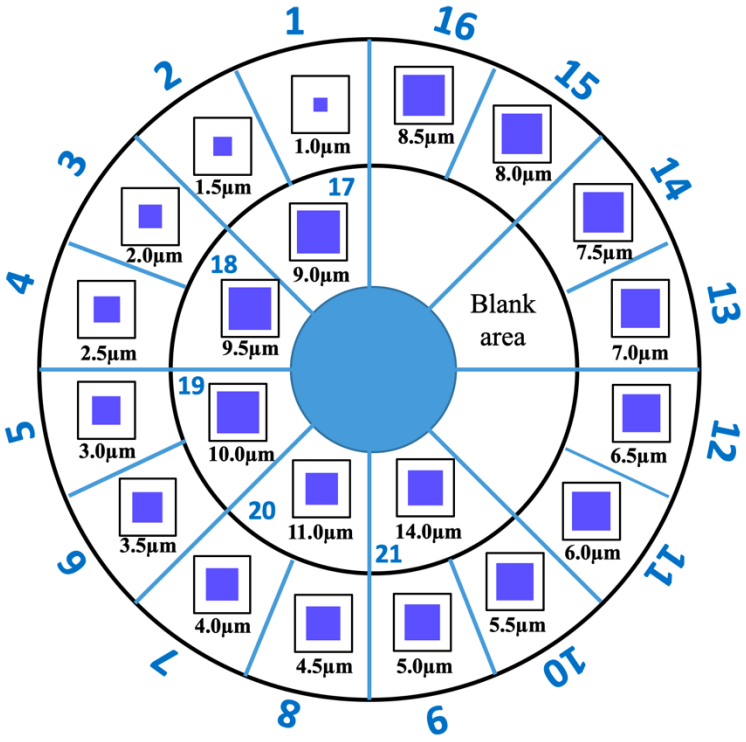

Figure 5. Layout used for the photolithography process for fabricating a set of metamaterial structures

B. FABRICATION

A multi metamaterial sample was fabricated by following standard microfabrication techniques [6]. The fabrication sequence is shown in Figure 6. A 550 µm thick of silicon wafer was used as the substrate (1), an 80 nm thickness of Al was deposited for use as the ground plane, and the Ångstrom Covap thermal metal evaporator was used to at chamber pressure 6.9 µTorr (2). Next, a 1.6 µm thickness of SiN_x metamaterial was

deposited onto the Al ground plane using the Oxford plasma lab system 100 machine. The plasma ICP power is set at 500 W while experiencing chamber pressure at 10.0 mTorr (3). The SiH_4 and Ar were set to flow at 50.0 sccm and 15.0 sccm, respectively, and the substrate was kept at 300 ºC. An 80 nm thickness of Al was deposited to serve as the resonator layer, and used the Ångstrom Covap thermal metal evaporator at a chamber pressure 6.9 µTorr (4). Prior to the deposit of the photoresist onto the top Al layer, a MicroChem (MCC) primer 80/20 was applied to remove moisture and prepare the surface. Next, around 1µm thickness of SPR 955 CM 0.9 photoresist was spun for 45 seconds at 3,000 rpm (5) and soft baked for 90 seconds at 90 ºC. The resonator was patterned using a photomask with 0.7 seconds UV exposure time using an EVG 620 mask aligner (6), and the resonator was then hard baked for 90 seconds at 120 ºC. The development was conducted by the MICROPOSIT MF CD-26 developer for 105 seconds. Finally, an Ar sputter etched the sample using the Oxford plasma lab system 100 (7). A Trion Sirius T2 oxygen plasma was used to clean the sample by removing the remaining photoresist. The plasma RF power was set at 250 W, and the oxygen was set to flow at 50 sccm.

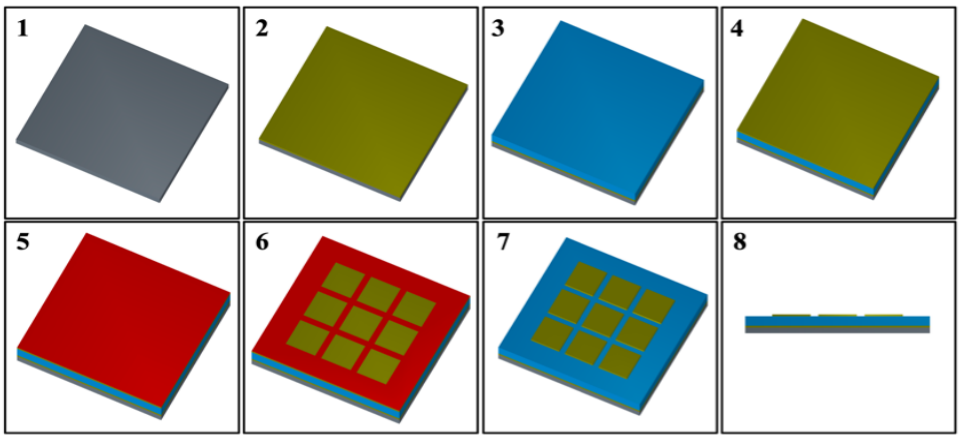

Figure 6. Schematics of fabricating sequence of a metamaterial

C. RESULTS AND ANALYSIS

The sample was fabricated following the MEMS microfabrication techniques. And the absorptivity of each metamaterial structures was measured by Fourier Transform Infrared Spectrometer (FTIR). Also, the dimension of each structures was measured for using as feedback into the finite element models. The finite element simulation was conducted, and the refractive index of SiN_x was investigated.

1. Fabrication of the Sample and Measuring Data

Figure 7 shows the fabrication results of the 21 sections taken. Only 11 sections out of the entire 21 got acceptable fabrication outcomes (e.g. 1.0 μm, 1.5 μm, 2.0 μm, 4.0 μm, 4.5 μm, 5.0 μm, 5.5 μm, 7.5 μm, 8.0 μm, 8.5 μm, and 9.0 μm.). A few factors may affect the bad outcome of some of these sections. One of the reasons is the sample contamination that can occur at any stage of the fabrication process, and this contamination can affect the final structures [7]. Another reason was the lack of a completely uniform deposition layer. During the process of deposition, the Al on the silicon substrate had a deposition rate that was unstable from time to time. Also, during the process of growing the SiN_x on the Al, the use of the Oxford plasma lab system 100 caused a rise in the temperature of the substrate, which could be a sizable factor in the final result. The uniformity of the dielectric layer may have also been compromised. In addition, the chemicals used for the photolithography may have suffered from factors such as being past their expiration date, and their quality could not be guaranteed. Several attempts were made and the best sample was used for the characterization.

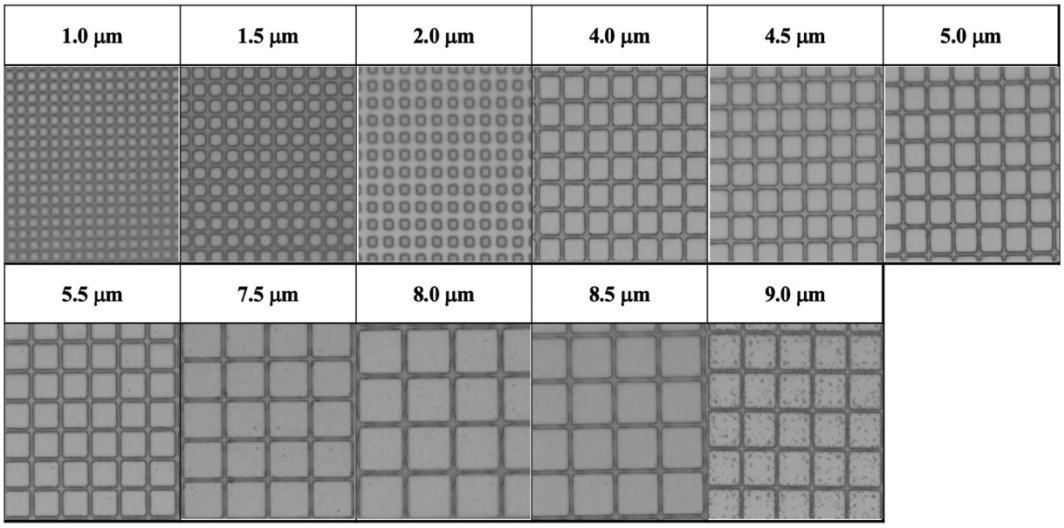

Figure 7. Micrographs of a set of fabricated metamaterials

The thickness of the Al ground plane, the thickness of the SiN_x dielectric material, and the thickness of the Al resonator were measured during the process. The Al ground plane thickness was 78.3 nm, the SiN_x dielectric material thickness was 1.590 μm, and the Al resonator thickness was 80 nm. The Al layer thickness was measured only at the center of the wafer by using a contact stylus profilometer, and this is because the metamaterial structures are located in the periphery of the sample. The optical properties, absorptivity and emissivity, were measured using a Thermo-Nicolet Nexus 870 FTIR. The transmissivity and reflectivity of the samples between 1.5 and 18THz were measured at each wavelength with a PIKE Technologies Mapp IR accessory of the FTIR. The gold film on the silicon wafer was used to collect the background for measuring reflectivity [3]. Figure 8 shows the results of the frequency dependent absorptivity and emissivity of all the measured sections with different size square resonators. This information is also included in Table 1 for comparisons with the simulation results.

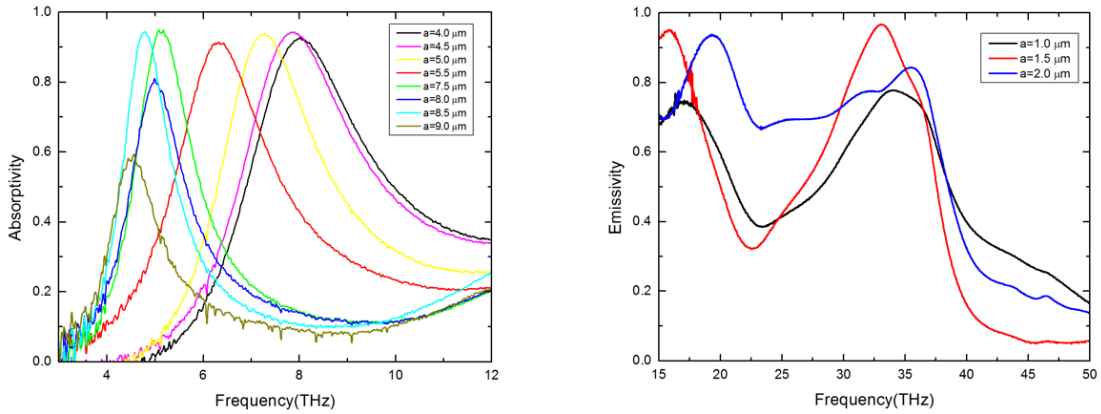

The graphs in (a) are used for finding the sub THz spectra range refractive index. The graphs in (b) are used for finding the IR spectra range refractive index. The resonator square size is represented as "a" in the legend.

Figure 8. Measured THz spectra

Starting from the resonator with its size of a = 9 μm, the frequency of the peak increases as the square size decreases down to 4 μm (shown in Figure 8 (a)). The magnitude of the response is smaller for structures with sizes of a = 9 μm and 8 μm, most likely due to the thickness of the SiN_x layer on these regions. It is known that thickness of the dielectric layer greatly affects the absorption magnitude in this kind of structures [8]. This fact does not, however, compromise the refractive index analysis. For square sizes smaller than 3 μm, it is difficult to predict the response, as SiN_x is highly absorbent in the LWIR band. Figure 8 (b) shows the response of three sections that followed this criteria. Nevertheless, it is possible that fitting can be attempted to match the curve shape and obtain the refractive indexes in this region.

Next, the feature sizes were measured (square resonators and gaps) using a calibrated microscope. Figure 9 and Table 2 show the actual dimension information of each resonator design and frequency, which has the first peak of the absorptivity and the emissivity. These data points are used to correct the finite element simulation.

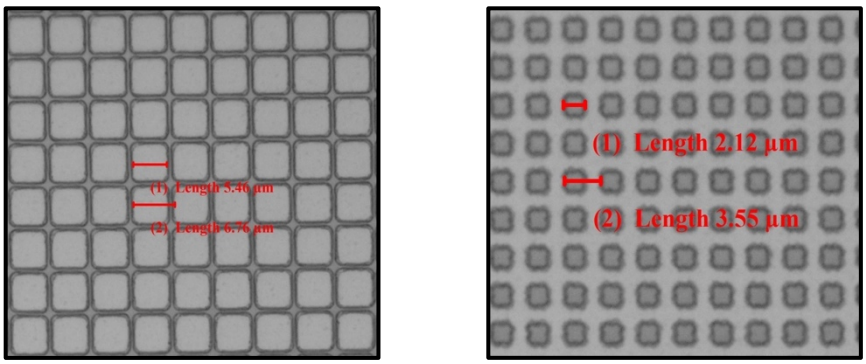

Figure 9. The measurement of the metamaterial dimension

Table 2. Dimensions of the metamaterials

Square size (µm)	Unit cell size (µm)	Gap (µm)	SiN_x thickness (µm)	1st peak freq. (THz)
1.38	2.45	1.07	1.520	34.105
2.05	2.985	0.935	1.530	32.818
2.09	3.49	1.4	1.597	19.486
4.55	5.75	1.2	1.570	8.009
4.85	6.2	1.35	1.597	7.954
5.39	6.55	1.16	1.597	7.275
6.02	7.31	1.29	1.595	6.425
8.12	9.22	1.10	1.578	5.084
8.39	9.7	1.38	1.545	5.000
9.07	10.36	1.29	1.519	4.798
9.28	10.77	1.49	1.597	4.441

2. Simulation Result and Silicon Nitride Refractive Index

The next step of finding the SiN_x refractive index is fitting the simulation result into the experimental data. The COMSOL model is using the dimension information that is shown in Table 2. Table 2 contains the actual measurement data of the fabricated sample. There is no SiN_x refractive index information within the sub-terahertz range. Because of this, the table is using only one estimated value of the real and imaginary parts of the

refractive index of the first peak of the absorptivity and the emissivity frequency for the simulation. The COMSOL automatically calculated the absorptivity and emissivity in other frequency ranges by using a constant refractive index.

It is important to give a brief reminder about the definition of the refractive index. The real part is related to the actual refraction. The real part of the refractive index was used to fit the peak resonance. As seen in Figure 10, increasing the real value of the refractive index causes the frequency to decrease. The real part of the refractive index value is inversely proportional to frequency. The imaginary part of the refractive index was used to roughly fit the possible width of the response. Increasing it will cause the response to be broader and lower in magnitude. The imaginary part of the refractive index is inversely proportional to the magnitude of the absorptivity and emissivity and is directly proportional to the width of the response.

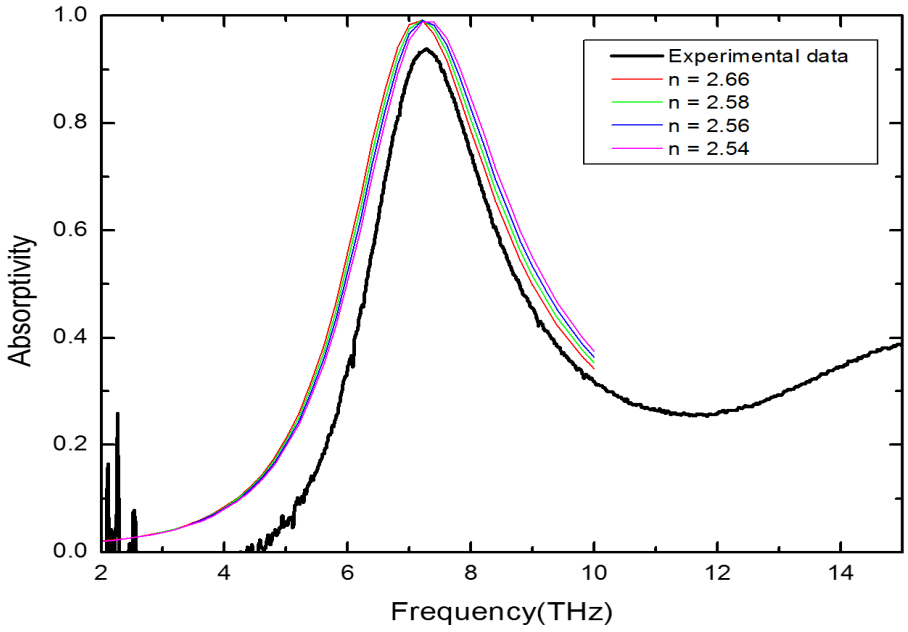

Figure 10. The result of absorptivity with the varying real value of the refractive index

The COMSOL simulation was conducted using data from Table 2 where both parts of the SiN_x refractive index were varied at each resonance to fit the experimental results.

This procedure made it possible to obtain the frequency dependent refractive index of our SiN_x films, shown in Figure 11. Figure 11 shows the results of the frequency domain SiN_x refractive index from 3 to 8 THz. The dashed regions are spline interpolations due to the lack of reliable metamaterial measurements in that range. The error for values greater than 9 THz is due to the lack of experimental data points in that region. Figure 12 shows the result of comparing experimental data to simulation results that use the refractive index data found in Figure 11. More experimental data is needed to improve the accuracy of the absorptivity results in the sub-terahertz range. This is planned as a future work.

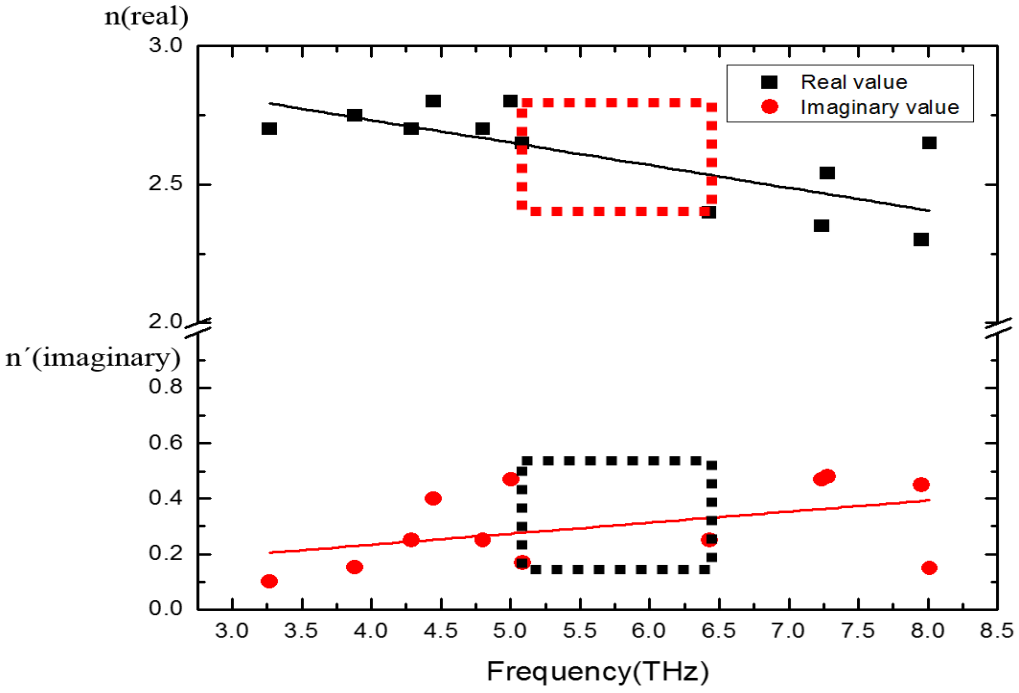

Figure 11. Fitted refractive index of SiN_x deposited by the PECVD at the NPS Clean Room

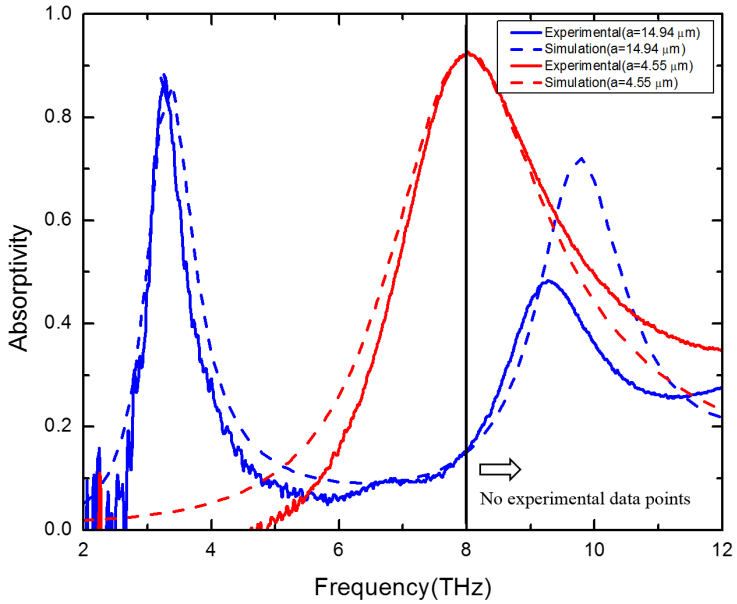

The solid line is the experimental data and the dash line is simulation results. The refractive index value from Figure 11 is used for the simulation. Two resonators are used in proving the refractive index value. The resonator dimension of the blue is a 4.55 μm square with a 1.5 μm gap. The red is a 14.94 μm square with a 3.5 μm gap.

Figure 12. Comparison of experimental and simulated absorptivity

Feeding back the obtained refractive index of SiN_x in the finite element simulations allows us to next concentrate our efforts into designing a highly efficient absorber in the THz range, and to design an emitter in the IR range of the camera used in the imaging system (see Figure 3).

THIS PAGE INTENTIONALLY LEFT BLANK

III. TERAHERTZ METAMATERIAL DESIGN

A. RESONATOR STRUCTURE FOR OPERATION AT 3.8 THZ

As previously mentioned, the NPS SRL has QCLs at 3.8 THz and 4.75 THz. The first structure will be designed to exhibit the highest possible absorption at 3.8 THz and to be as narrow as possible.

The initial approach is to use the geometry found in Alves et al. [4]. In this paper, they studied the creation of perfect absorbers using silicon oxide as the dielectric material and used a single square. The geometry of the first designed unit cell, called unit cell A, is shown in Figure 13.

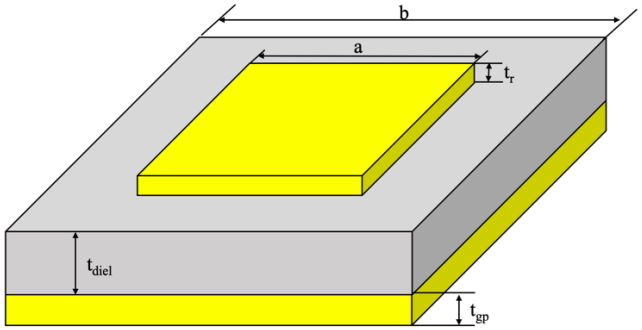

Figure 13. The geometry of unit cell A

The unit cell size is defined as B, the resonator size is defined as A. The 80 nm thickness of aluminum is used for the ground plane and the resonator. The 1600 nm thickness of silicon nitride is used as the dielectric material. There were only two varying parameters—unit cell size and resonator size.

Two aspects were considered in designing this structure. First, the peak resonant frequency should be adjusted to be as close as possible to 3.8 THz. This was done by starting the simulation with the resonator size set at 11 μm and the unit cell size set at 15 μm. The resonator size was varied throughout the experiment, and the initial results are shown in Figure 14.

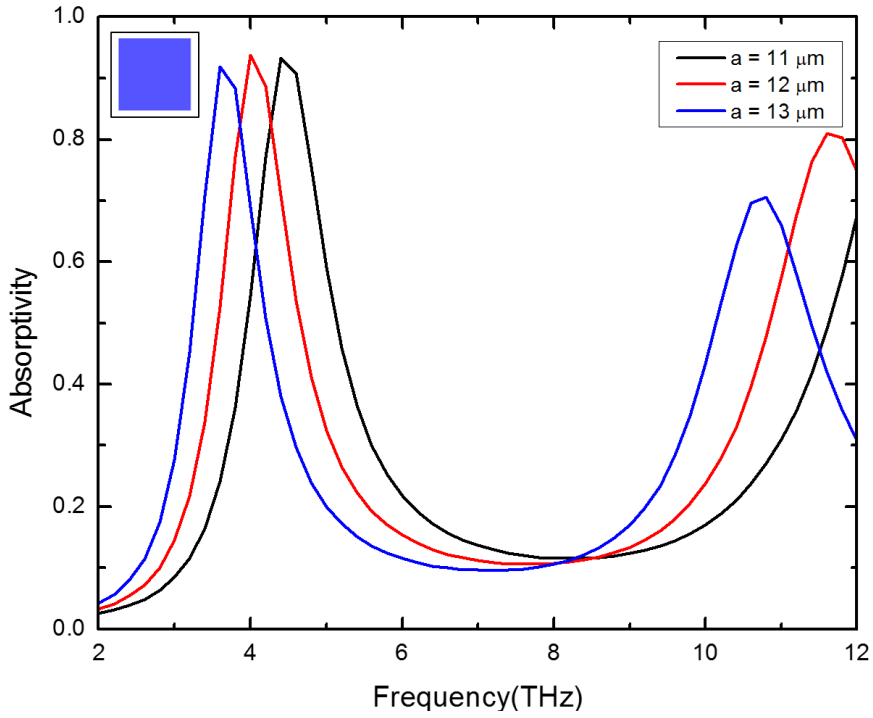

Figure 14. Absorptivity with varying resonator square sizes keeping unit cell size of 15 μm

The closest simulated value was obtained by using a 13 μm square resonator (3.6 THz). The next step was to optimize the fill factor, defined as the ratio between the resonator size and the unit cell size. Knowing that the fill factor slightly affects the resonant peak [4], this was performed before further adjusting the square size. In addition, the higher fill factor increased the absorption magnitude [9].

Figure 15 shows that the fill factor is inversely proportional to the frequency. This is only varied in very small gaps [8]. This indicates that the fill factor can be adjusted for the resonator size of 13 μm to tune the unit cell to 3.8 THz. As shown in Figure 15, the fill factor of 66.1 % achieved by a unit cell size of 15 μm will provide peak resonance at 3.8 THz.

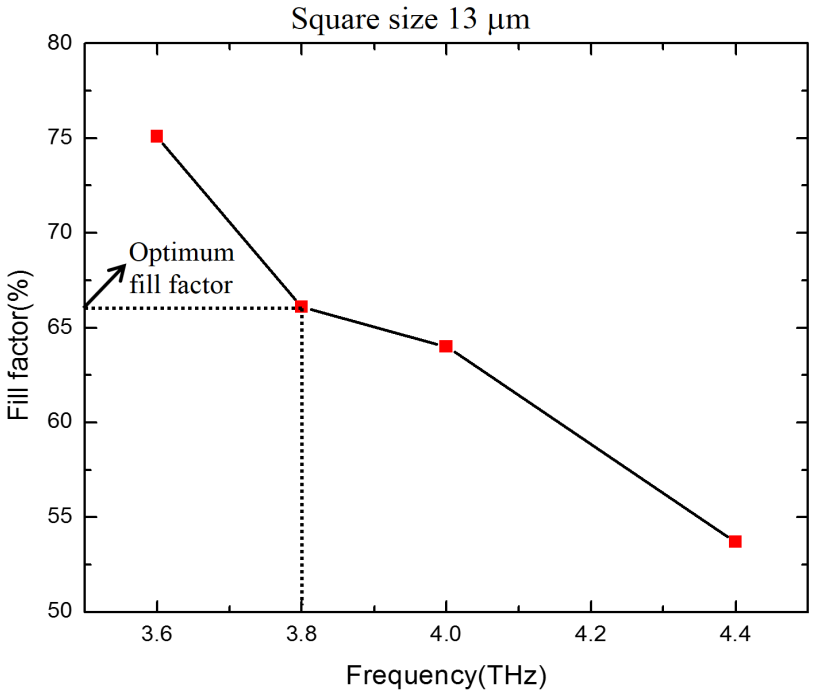

Figure 15. Variation of fill factor with frequency

Table 3 summarizes the experiment and its results. Figure 16 shows the final simulated results and parameters for the 3.8 THz perfect absorber. Using this result, the metamaterial for the terahertz side was fabricated as described in chapter 2.

Table 3. Unit cell A geometries used in the simulation

	a (μm)	b (μm)	Fill factor (%)	1st peak Freq. (THz)	Absorptivity (%)
Vary a	11	15	53.7	4.4THz	93.1
	12	15	64	4.0THz	93.7
	13	15	75.1	3.6THz	91.8
Vary b	13	16	66.1	3.8THz	92.2
	13	17	58.5	3.8THz	89.6
Optimized	13	16	66.1	3.8THz	92.2

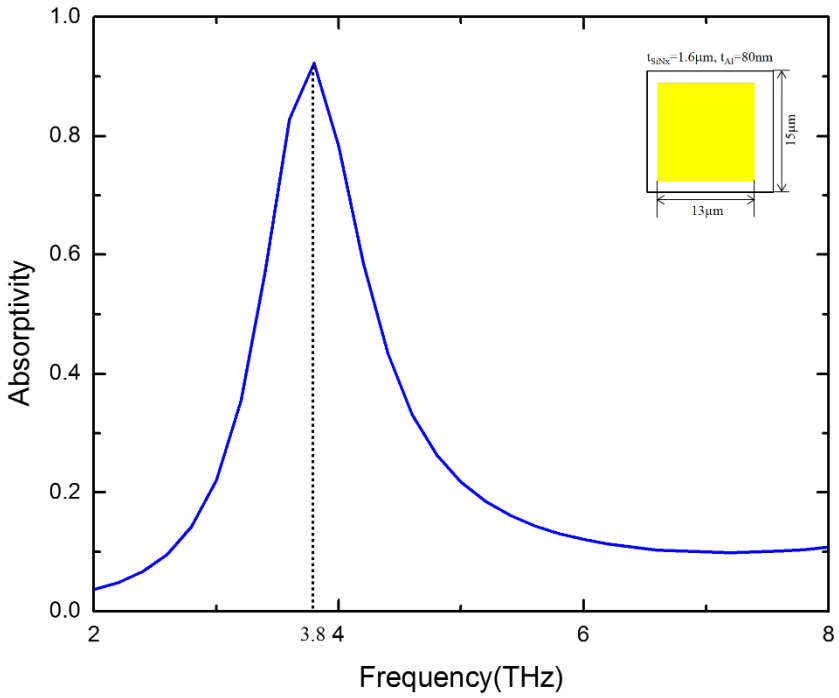

Figure 16. Simulated absorptivity for the 3.8 THz perfect absorber

Table 4 shows the fabrication result of unit cell A. The ground plane was a deposited 78.3 nm thickness of aluminum. The 1.63 μm thickness of silicon nitride was grown on the aluminum ground plane. After that, an 80 nm thickness of aluminum was deposited on the dielectric material to serve as the resonator. The fabricated unit cell and the resonator square size are slightly different from the original design. There is a 0.77 μm difference in the size of the resonator and a 0.59 μm difference in the size of the unit cell. The entire geometry of unit cell A has slightly shrunk.

Table 4. Unit cell A geometries

	Al thickness(nm)		SiN_x thickness(μm)	a (μm)	b (μm)	1st peak Freq. (THz)
	Ground	Resonator	Dielectric			
Experimental	78.3	80	1.63	12.23	15.41	3.82
Simulation	80	80	1.60	13	16	3.80

Figure 17 shows the results of the experimental and the simulation tests of unit cell A. The top-left side of the graph shows the picture of the fabricated sensor image. The two graphs are nearly identical. The absorptivity and the first peak frequency values are nearly identical. The width of the simulated response is around the frequency of 3.8 THz and is slightly wider than experimental one, however, it is within 1 % error range and it does not compromise the design. Overall, the configuration was selected to be the 3.8 THz illumination source.

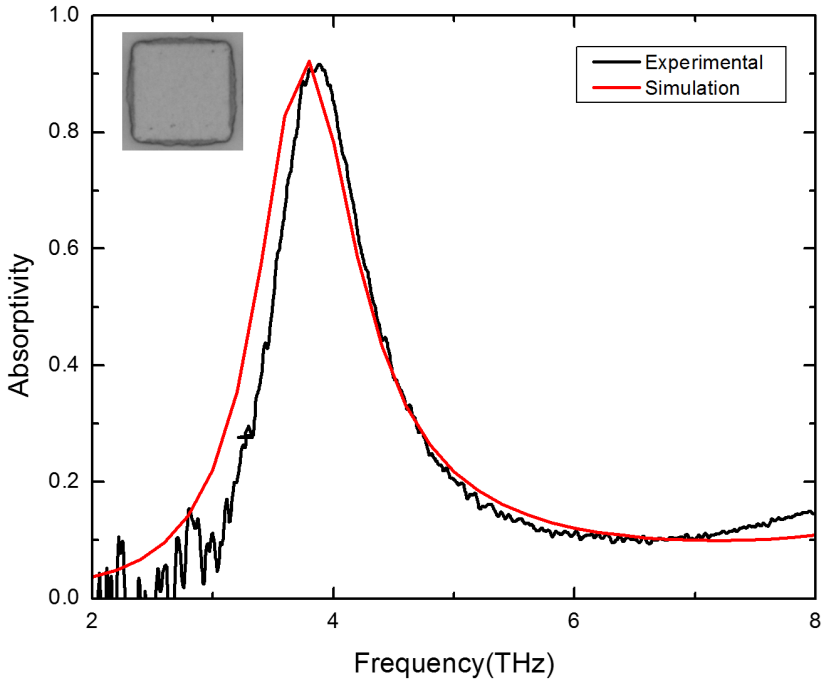

Figure 17. Measured and simulated absorptivity of unit cell A

B. RESONATOR STRUCTURE FOR OPERATING AT 4.75THZ

The same procedure used to design the metamaterial structure with an optimum absorption of 3.8 THz was used to design a structure intended for 4.75 THz. Knowing that the frequency of the peak absorption is inversely proportional to the square size [4], we started the simulation by varying the square resonator size from 8 to10 μm with a fixed unit cell size of 11 μm, called unit cell B. Next, the unit cell's size was varied from 10 to

11 μm. Table 5 summarizes the simulation runs and results. The configuration that provided the most efficient absorption at 4.75 THz was a resonator size of 9.0 μm, a unit cell size of 10.0 μm, and a peak absorptivity of 93.4 %. Figure 18 shows the final simulated results and parameters for the 4.75 THz perfect absorber. Using this result, the metamaterial for the terahertz side was fabricated.

Table 5. The geometry and the simulated data for unit cell B

	a (μm)	b (μm)	Fill factor (%)	1st peak Freq. (THz)	Absorptivity (%)
Vary a	8	11	52.9	5.8THz	93.6
	9	11	66.9	5.0THz	93.4
	10	11	82.6	4.2THz	91.0
Vary b	9	10	81.0	4.6THz	94.1
	9	10.5	73.4	4.75THz	93.4
Optimized	9	10.5	73.4	4.75THz	93.4

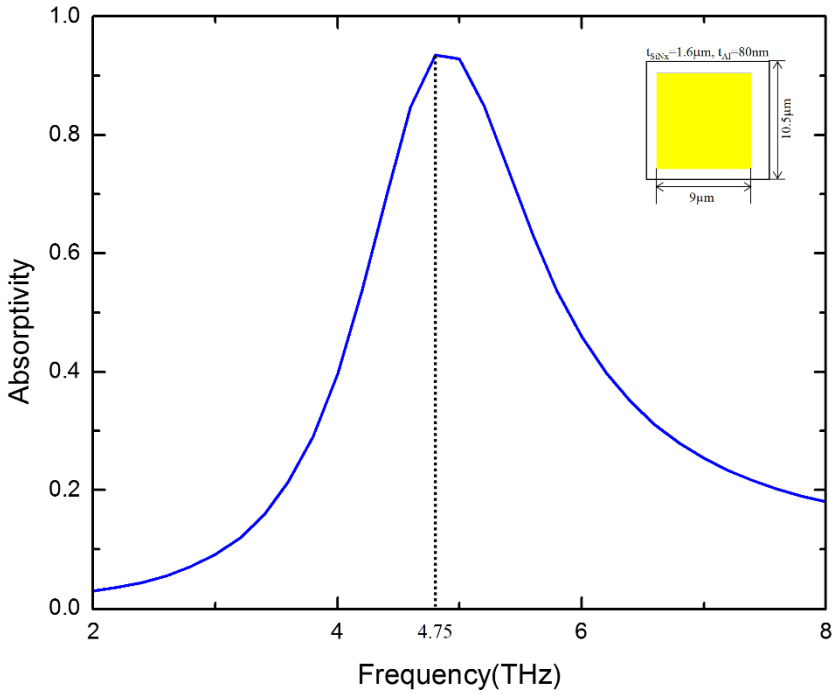

Figure 18. Simulated absorptivity for the 4.75 THz perfect absorber

The sample was fabricated using same method that was mentioned above. Table 6 explains the geometry of unit cell B. The fabricated sample has a 78.3 nm aluminum thickness for a ground plane, an 80.0 nm aluminum thickness for a resonator and a 1.519 μm silicon nitride for a dielectric layer. The square size is 9.07 μm and the unit cell size is 10.36 μm. The resonator square is slightly larger than the simulation design and the unit cell is slightly smaller than the simulation design. As it can be seen in Table 6, the small fabrication discrepancies did not affect the resonant peak.

Table 6. Unit cell B geometries

	Al thickness(nm)		SiN_x thickness(μm)	a (μm)	b (μm)	1st peak Freq. (THz)
	Ground	Resonator	Dielectric			
Experimental	78.3	80	1.519	9.07	10.36	4.75
Simulation	80	80	1.60	9	10.5	4.75

Figure 19 shows the experimental results and the simulation results of unit cell B. The picture located in the upper-left side of graph is the fabricated result. The simulated response is slightly broader than the measured response. This configuration was selected to be the absorption layer for the 4.75 THz illumination source.

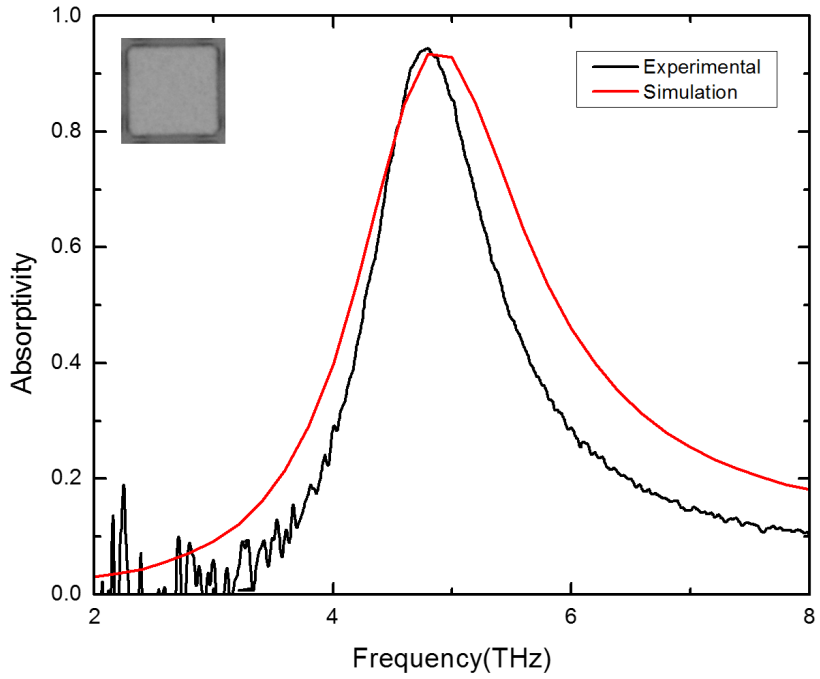

Figure 19. Measured and simulated absorptivity for unit cell B

IV. FINITE ELEMENT MODELING FOR IR EMITTER

For improving the conversion efficiency, the emissivity of resonator has to reach nearly 100% in the interest frequency region between 20 and 40 THz (7.5 – 14 μm), while emissivity should be nearly zero out of these frequencies. The CST Microwave Studio was used to perform the simulations in a unit-cell basis. This is similar to what was performed in COMSOL for the THz absorber. The phase reflection workflow and frequency domain solver functions were used for the simulation [10].

The metamaterial unit cell (Figure 20) is sandwiched by two wave guide ports – Z_{max} and Z_{min}. The electromagnetic wave propagates to the metamaterial surface that is sent from Z_{max} with the direction perpendicular to the cell. Scattering parameter S_{11} was extracted over a wide frequency range. Reflectivity is given by $|S_{11}|^2$. Since the second order scattering is negligible for the feature dimensions of these structures, emissivity can be estimated as $1-|S_{11}|^2$.

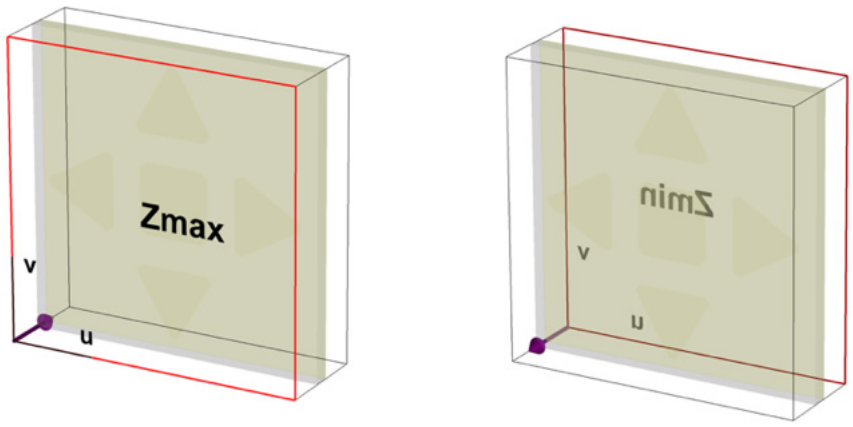

Figure 20. Schematic diagram of the unit cell used for CST simulation

A. PROPERTIES OF SILICON NITRIDE PROPERTY IN LWIR RANGE

In this range, the SiN_x refractive index can be obtained from several open literature publications, however, none represents the exact properties of the film grown at NPS. An attempt to fit the properties to CST, starting with the values obtained in the literature [11] for a unit cell shown in Figure 21, was made. Initially, the structure shown in Figure 21 was fabricated (see inset of Figure 22) and measured (Figure 22 – black solid line). The simulated structure response using the refractive indexes given in the literature is shown in red. The fitting attempt is shown in blue, and the fitted refractive index was used for the design. The idea was to concentrate on the spectral characteristics of the response, rather than on the magnitude, to obtain a degree of high selectivity.

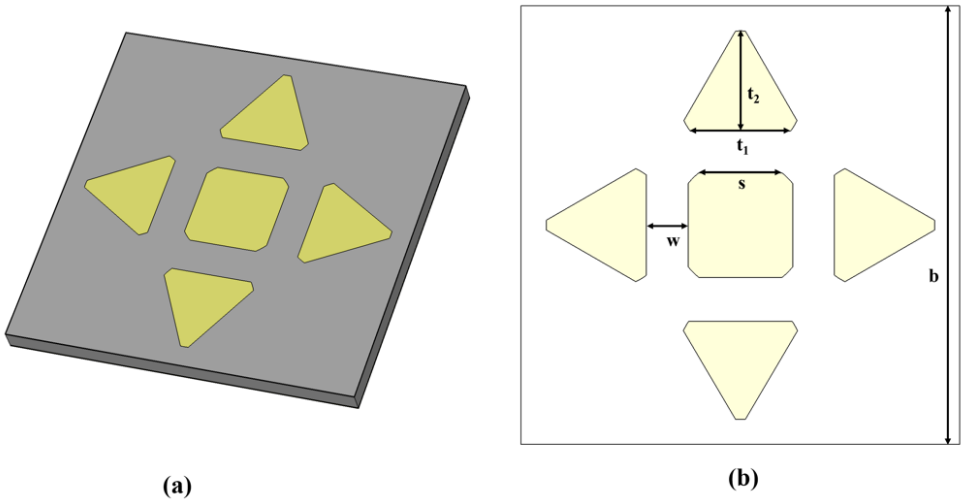

(a) The metamaterial design for finding the SiN_x refractive index information in broadband IR. The metamaterial design includes a square and triangles. The main characteristic of design is the round vertex. The sharp vertex is difficult to fabricate during the MEMS microfabrication process. (b) The symbols were used for delivering the dimension information of the resonator structures.

Figure 21. Unit cell design for finding SiN_x properties in LWIR

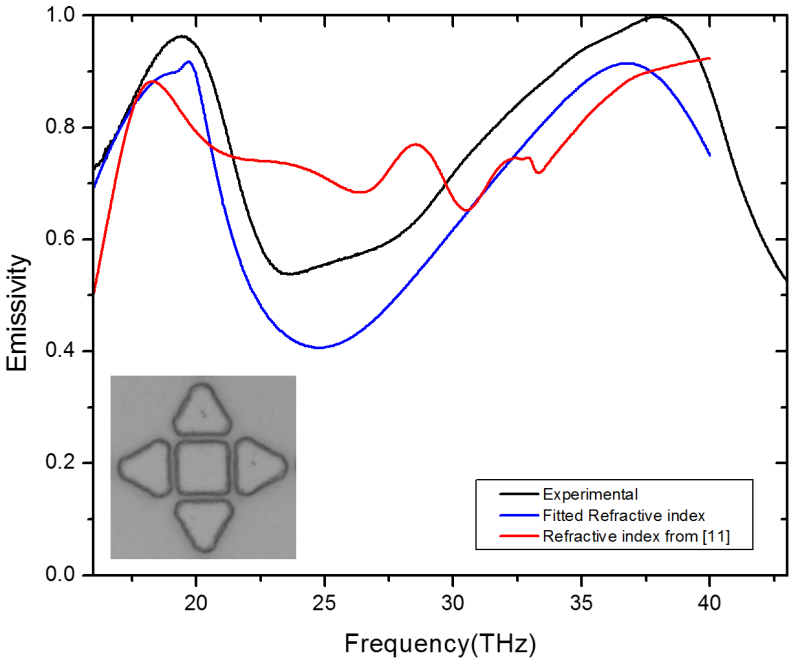

Figure 22. Comparison of the simulation results with the experimental data

B. RESONATOR DESIGN USING DIFFERENT DIELECTRIC MATERIAL THICKNESS

It is known that thickness of the dielectric layer greatly affects the emission magnitude [8]. The six different structures were studied to find perfect emitter for the imaging system with varying the thickness of SiN_x.

1. 1.6 μm Thickness of The Silicon Nitride

In this chapter, six different resonators designs were studied to select the best configuration for the emission layer of the imaging sensor. The six different resonators design were denoted as unit cells C, D, E, F, G and H. Three different geometries, such as square, triangle, and circle, were incorporated in the making of the metamaterial structures. An 80 nm thickness of aluminum was used for the ground plane and resonator. A 1600 nm thickness of silicon nitride was used for the spacer between the resonator and the ground plane.

Figure 23 shows the unit cell C, D and E structures. Unit cell C geometry was selected from Gong et al. [11]. In this paper, asymmetric geometries were used for studying that is deformed from the unit cell C. In the unit cell C, the single square ring was used for the metamaterial structure. The unit cell size is 21 μm, the outer border is 18 μm, and the inner border is 15 μm. In the unit cell D, two square rings were used. The unit cell size and the external ring size are the same as the sizes used in unit cell C. The inner border size is 12 μm, and the width is 1.5 μm. Unit cell E's metamaterial structure consists of five squares. The unit cell size is 20.5 μm, the length of center square size is 8 μm, and the other four squares have the same length of 4 μm.

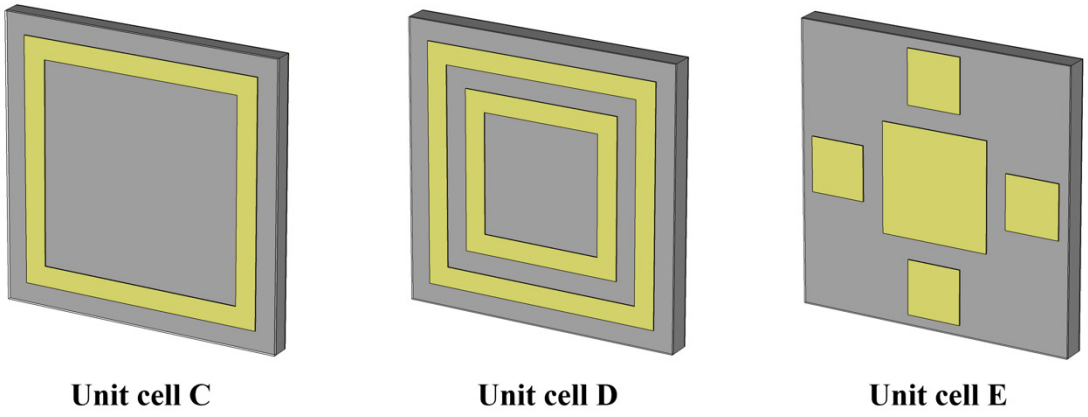

Figure 23. Unit cells C, D, and E used in finite element modeling

Figure 24 shows the emissivity response of unit cells C, D, and E. Unit cell C has higher emissivity response in all frequency regions than the other two unit cells. All the unit cells have a similar peak resonance around 17 THz. They exhibit the lowest emissivity response around 22 to 25 THz. Even though, unit cell C and unit cell E have different metamaterial structures, their emissivity response on that frequency range (22 to 25 THz) is similar. These results lead to the conclusion that the silicon nitride properties strongly affect the emissivity response around 17 to 25 THz, and these properties serve as the predominant source of absorption. The emissivity response can be changed by varying the silicon nitride thickness [8].

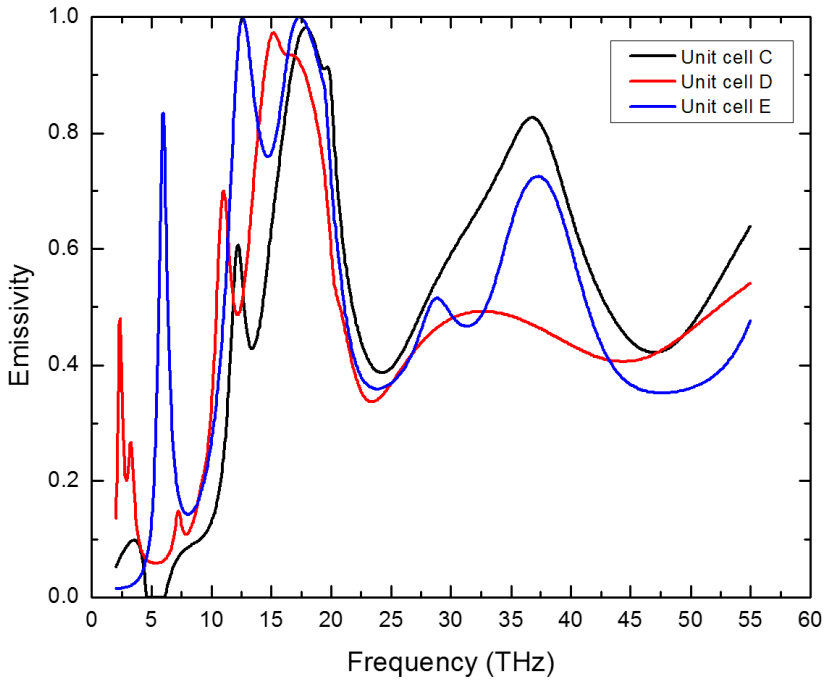

Figure 24. The simulation emissivity of unit cells C, D, and E

Figure 25 shows unit cells F, G and H's metamaterial structures. Unit cell G has the same geometries as unit cell F. Four triangles and a square were incorporated in the construction of unit cell F. The difference between unit cells F and G is the vertex shape. All the vertices in unit cell G were round filleted. The basic structure design of unit cell H is the same as the shape of unit cell G. The difference between unit cells G and H is that a circle was used for the unit cell H instead of a square.

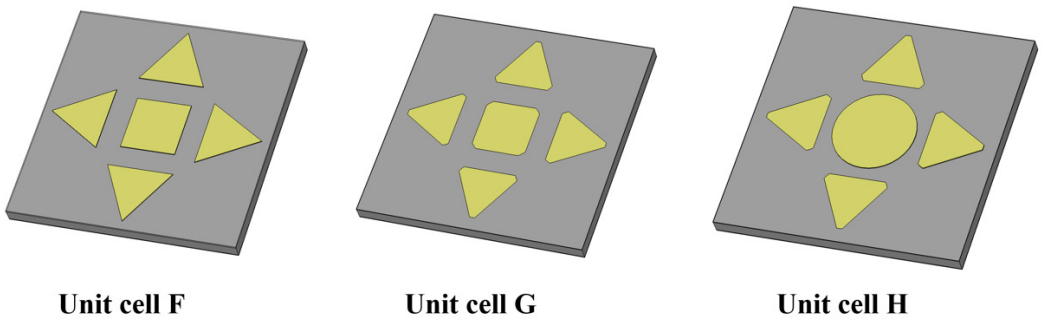

Figure 25. Unit cells F, G, and H used in finite element modeling

Figure 26 shows the nomenclature used to design the structures, and Table 7 shows the size of each metamaterial structures. Each unit cell size is 21 μm. The size of the triangles in unit cells G and H are the same, but the size of the triangles were reduced compared to the triangles used in unit cell F due to the round vertices. The gap between the geometries is 1.5 μm for unit cells F and G. Unit cell H has a 1.0 μm gap. The gap of unit cell H is smaller than the others because the circle size was increased, but the unit cell size was the same. The critical dimension was kept at 1μm due to the fabrication limitations.

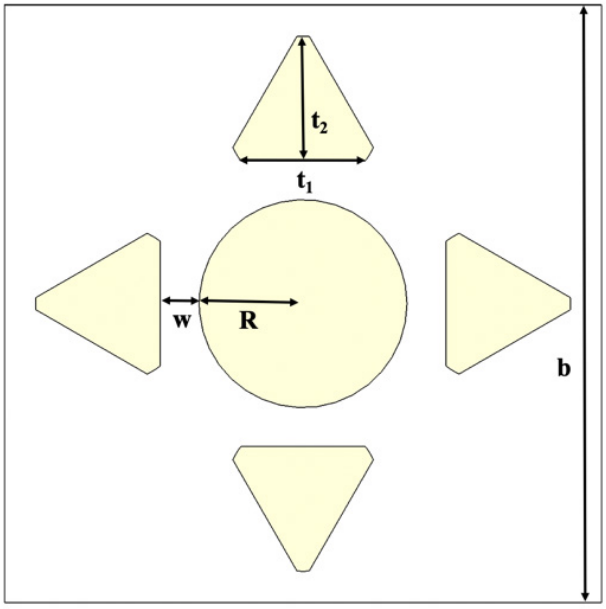

Figure 26. Unit cell H design parameters

Table 7. The geometries of unit cells F, G, and H

Unit cell F (μm)					Unit cell G (μm)					Unit cell H (μm)				
t_1	t_2	s	w	b	t_1	t_2	s	w	b	t_1	t_2	R	w	b
6	5.2	5	1.5	21	5.2	4.8	4.2	1.5	21	5.2	4.8	3.5	1.0	21

The simulation results of unit cells F, G, and H are shown in Figure 27. The emissivity response of these three unit cells exhibit similar results around 17 to 23 THz. These results are also similar to unit cells C, D and E. The response around 25 to 40 THz is higher for unit cells G and H. Unit cell G has the highest emissivity response from 25 to 40 THz, but it has the lowest emissivity response around 20 THz. Based on the result, it is difficult to select what is the best resonator design for the perfect IR emitter. Therefore, the two best results – unit cells G and H - will be used for further studying.

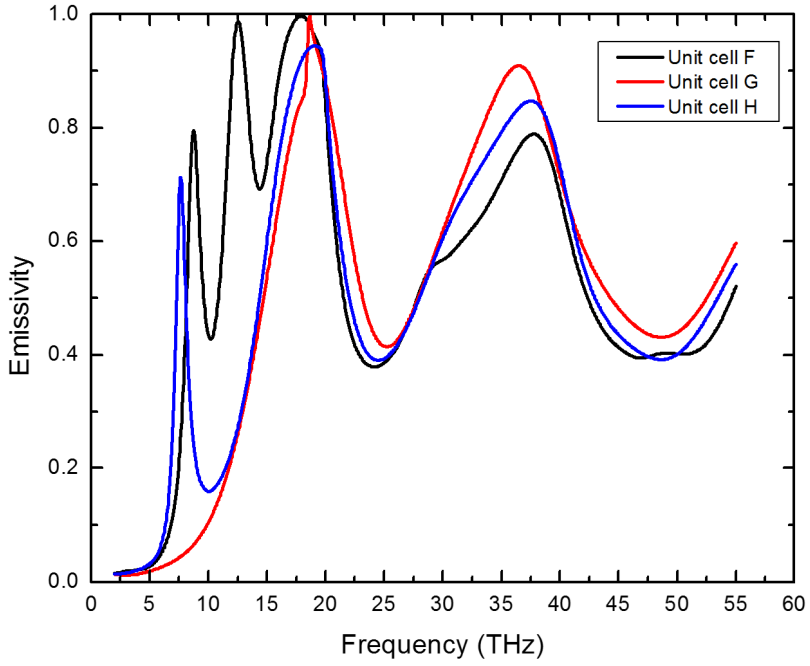

Figure 27. The simulated emissivity of unit cells F, G, and H

2. Varying Silicon Nitride Thickness

In order to understand the influence of SiN_x on the metamaterial absorption, finite element simulations were conducted using unit cells without an aluminum resonator. A 21 μm unit cell, with an 80 nm of Al as the ground plane and the SiN_x varying from 0.8 to 1.6 μm with 0.2 μm steps. The emissivity responses are shown in Figure 28. It can be observed that the peak resonant frequency increases as the thickness of SiN_x decreases. The peak resonant frequencies experienced a blue-shift during the simulation (20 THz, 21 THz, 22.5

THz, and 25 THz). This shows that in this spectral region, SiN_x per Si is a good absorber and the metamaterial configuration should be used only to tailor the response towards the desired requirements.

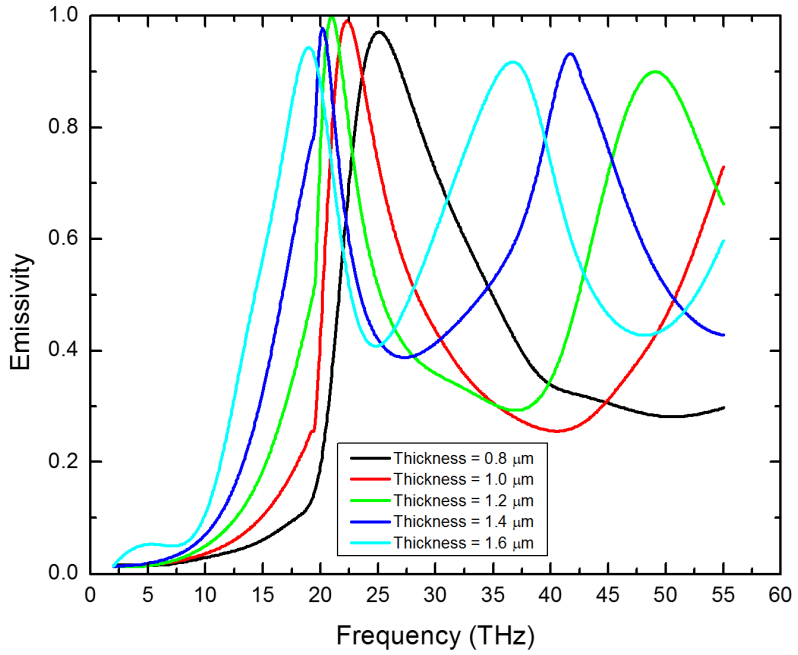

Figure 28. The emissivity for a set of dielectric material thicknesses

Since a nice cut-off at about 20 THz is shown for 1.2 μm thick SiN_x, unit cells G and H were re-simulated with changing dielectric material thickness ranging from 1.6 μm to 1.2 μm.

Figure 29 shows the simulated emissivity responses of unit cells G and H with 1.2 μm thickness of dielectric material. Notice that as the thickness reduces the effects of the metallic resonator (the peak resonance due to resonator dimensions) have increased in frequency from 25 to 40 THz. This response is not desired. This result indicates that the unit cell would potentially have regions with different thicknesses, and each region may favor specific spectral features.

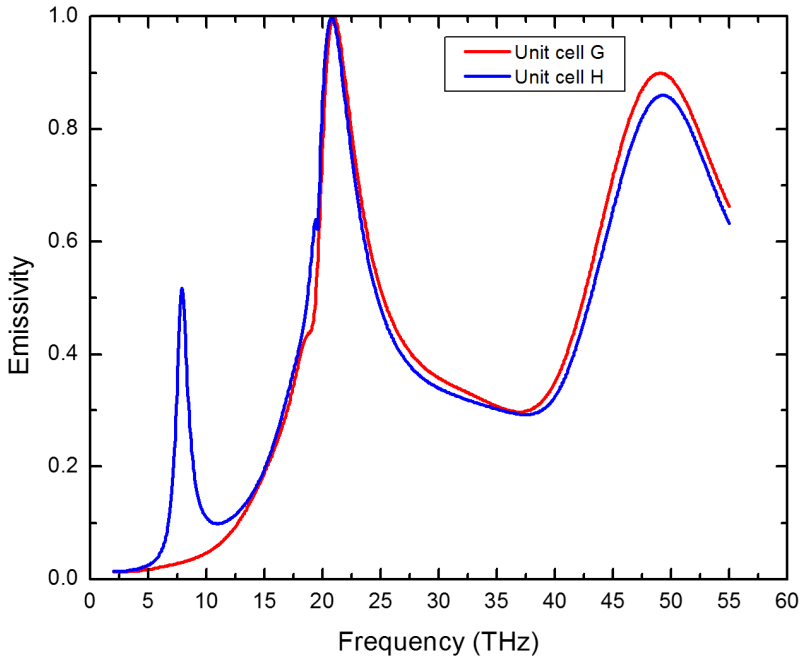

Figure 29. The simulated emissivity of unit cells G and H with a 1.2 μm thick dielectric layer

3. Unit Cell with Inhomogeneous SiNx Thicknesses

Several combinations of the unit cells G and H were simulated with different SiN_x thicknesses, such as greater central resonator region thickness than the rest of the cell, the opposite, configuration, and some other variants.

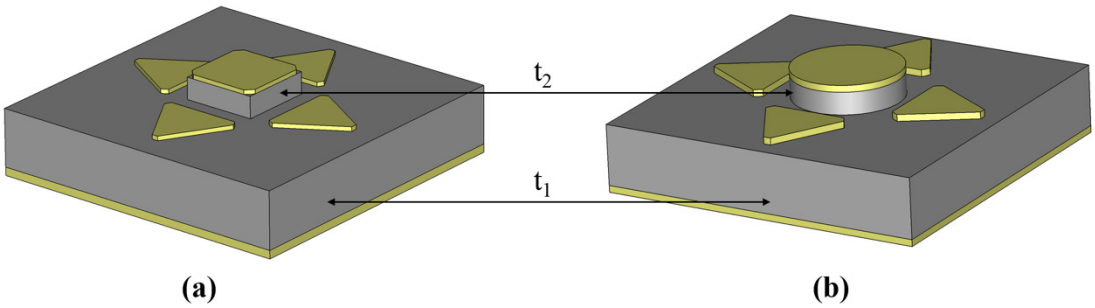

Figure 30. The schematic diagram of unit cells G and H with two different SiN_x layer thicknesses

Figure 31 shows the simulation results of unit cells G and H using dielectric material with two different thicknesses, and they were compared with the responses of unit cells G and H which were using 1.2 μm thickness layers of SiN_x. The black line shows the emissivity response of unit cell G, and the red line shows the emissivity response of unit cell H. The solid line is the result of using two different thickness of SiN_x and the dash line is the result of using a 1.2 μm thickness of single SiN_x. Although the emissivity response of SiN_x which different degrees of thickness layers is slightly improved, the region is not applicable.

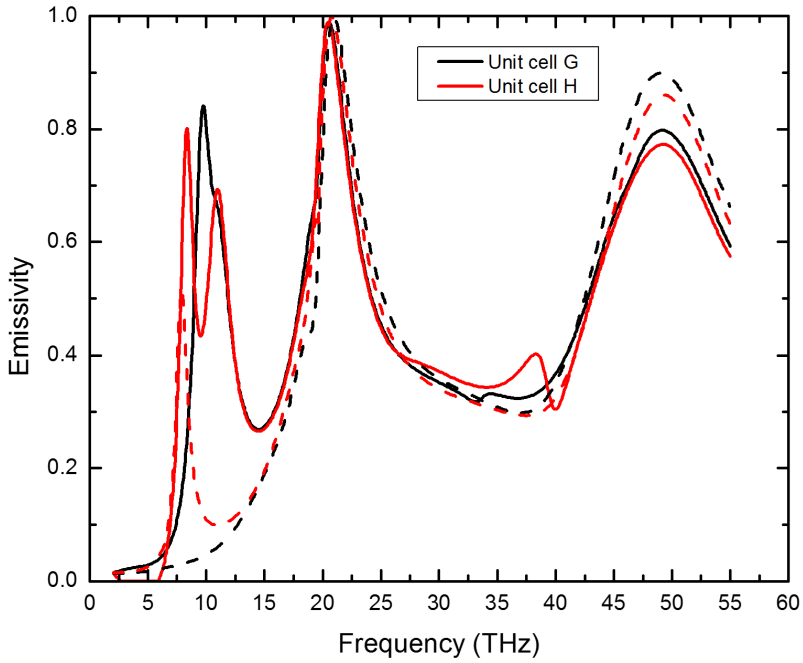

Figure 31. Simulated emissivity of unit cells G and H using two different thickness of SiN_x

The 1.6 μm thick SiN_x area was extended in an attempt to improve the emissivity response to around 30 to 40 THz, where the triangle vertices may match. Figure 32 shows the simulation results. The emissivity responses were improved in frequency range we were interested in, but the peak emissivity frequency is below 20 THz and the magnitude is below 80% over the entire range of our interest.

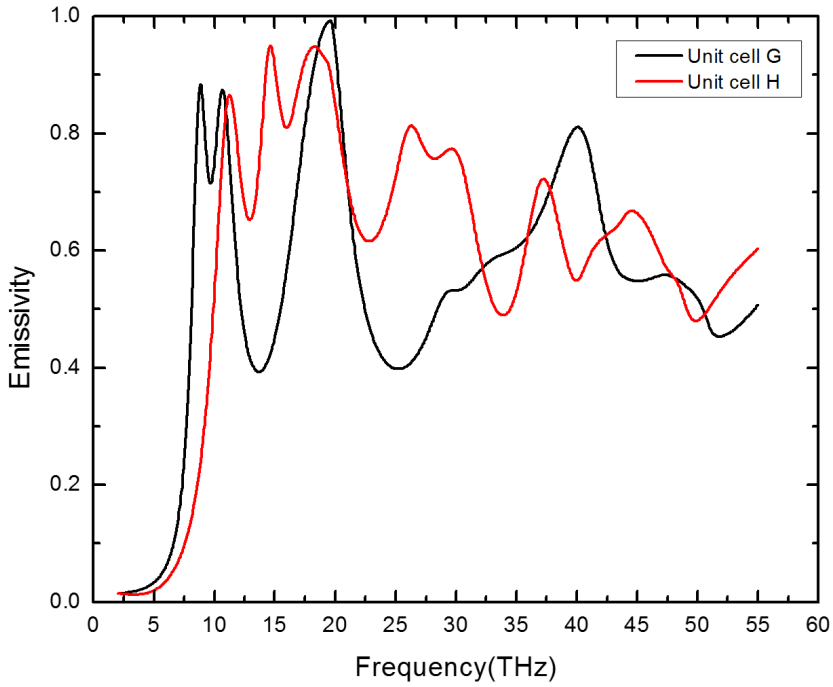

Figure 32. The emissivity of unit cells G and H with expanded 1.6 μm thick SiN_x

The SiN_x was next simulated with three different degrees of thickness. Figure 33 describes how three different thickness of SiN_x were configured in unit cells G and H. The thickness of the bottom SiN_x layer is denoted t_1, the thickness of the middle SiN_x layer is denoted t_2, the thickness of the top SiN_x layer is denoted t_3. The middle layer matched with the triangle vertex. Two different thickness values were used for this simulation. At first, $t_1 = 1.0$ μm, $t_2 = 0.2$ μm, and $t_3 = 0.4$ μm. Following this, $t_1 = 0.8$ μm, $t_2 = 0.2$ μm, and $t_3 = 0.6$ μm. The idea is that the SiN_x area ($t_1 + t_2$) would enhance the emissivity response in the frequency range of 20 to 25 THz, and the SiN_x area ($t_1 + t_2 + t_3$) would enhance the response in frequency range of 30 to 40 THz.

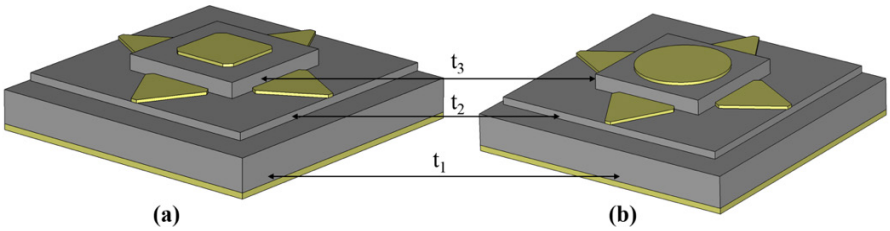

Diagram (a) shows unit cell G and (b) shows unit cell H. The symbols represent thickness of SiN_x layers. The square or circle area in the unit cell has 1.6 μm thickness ($t_1 + t_2 + t_3$) of SiN_x. Beyond this, 1.2 μm or 1.0 μm thickness (t_1 and t_2) of SiN_x was grown in the rest of area.

Figure 33. Unit cells G and H using three different layers of SiN_x

Figure 34 shows the emissivity response of each metamaterial design. The black line is the emissivity results of unit cell G, and the red line is the emissivity results of unit cell H. The entire set of emissivity responses in our frequency range of interest is slightly improved. Both designs have nearly the same emissivity responses in frequency from 20 to 25 THz and have good emissivity responses in frequency from 20 to 40 THz.

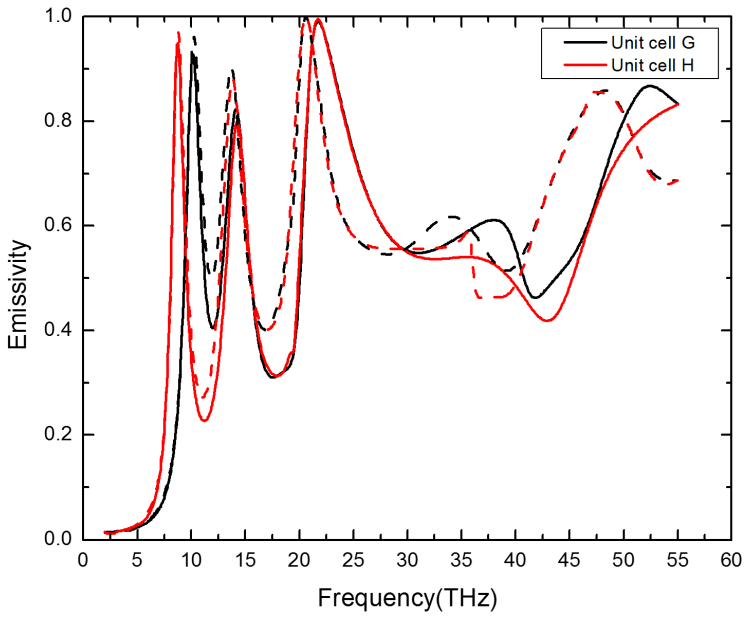

The dash lines are the emissivity results of two unit cells with $t_1 = 1.0$ μm, $t_2 = 0.2$ μm, and $t_3 = 0.6$ μm. The solid lines are the emissivity results with $t_1 = 0.8$ μm, $t_2 = 0.2$ μm, $t_3 = 0.4$ μm.

Figure 34. Simulated emissivity of unit cells G and H with three different layers of SiN_x

A simple efficiency calculation can be performed to help selecting the best configuration. Conversion efficiency is defined as the ratio of the energy emitted in the IR camera spectrum range (20 – 40 THz) and the total energy. In our case, this is considered to be between 2 to 55 THz. This can be obtained by dividing the integrals of the emissivity over the respective frequency ranges. Table 8 shows the conversion efficiency results of each unit cell. Unit cell H has a higher conversion efficiency than unit cell G. The best result is achieved by having unit cell H use 0.8 μm, 1.0 μm, and 1.6 μm thickness layers of SiN_x layers. Therefore, this metamaterial was selected to be fabricated as the IR emitter of the THz-to-IR converter.

Table 8. Conversion efficiency of unit cells H and G

	Unit cell G(μm)		Unit cell H(μm)	
SiNx thickness	t_1=0.8, t_2=0.2, t_3=0.6	t_1=1.0, t_2=0.2, t_3=0.4	t_1=0.8, t_2=0.2, t_3=0.6	t_1=1.0, t_2=0.2, t_3=0.4
Efficiency	45.88%	41.95%	47.26%	44.32%

Figure 35 shows the absorptivity and emissivity response of unit cell H using Si_3N_4 dielectric material. The refractive index of Si_3N_4 was used in open literature sources [5]. The emissivity responses in frequency from 20 to 40 THz are better than suggested. This finite element simulation result also allows us to concentrate our next efforts into fabricating a highly efficient IR emitter.

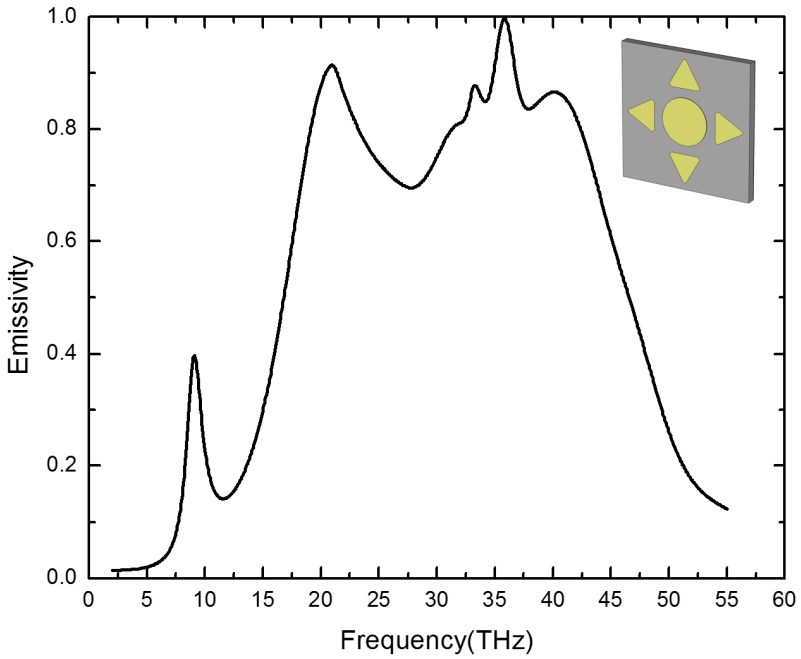

The finite element simulation of the metamaterial unit cell H was selected to be the IR emitter for the THz-to-IR converter using the parameters of the stoichiometric Si_3N_4 extracted from [5].

Figure 35. Simulated emissivity of unit cell H using Si_3N_4 as dielectric material

Note that the emissivity of the structure is greater than 0.8 at almost all points of the LWIR band. This interesting possibility should be further investigated.

V. CONCLUSION

The NPS SRL is developing MEMS THz-to-IR converters based on metamaterial perfect absorbers for real time imaging. The idea is to have a simple attachment that may be added to commercial-off-the-shelf LWIR cameras to expand the imaging capabilities to the THz frequencies of available illumination sources. The combination of these tools can be used in many applications, such as security screening, non-destructive evaluation, food inspection, and much more. The converters will be comprised of a back-to-back double-metamaterial structures uncoupled by a shared ground plane, and they are meant to be fabricated at the NPS microfabrication facilities (Clean Room) using the available processes. This study focused on designing two planar metamaterial structures that will be part of the converter. The first is the THz absorber, which maximizes the absorptivity of two quantum cascade lasers available in the sensor research laboratory, and minimizes absorptivity elsewhere in the THz spectrum. The second is the IR emitter, which maximizes the emissivity on the band of the LWIR camera and minimizes it elsewhere in the IR spectrum.

In this research, Al/SiN_x/Al metamaterial structures were used for the first time at NPS. Because of this, the properties of the metamaterial and its constituents had to be investigated. Throughout the research, metamaterial films were fabricated using metal evaporation, PECVD (Plasma enhanced chemical vapor deposition), sputter etching, and standard photolithography. Metamaterial films with 21 different resonators square sizes were designed, fabricated, and characterized in order to provide data to feedback into the finite element models used for the design. The refractive index in the regions of the spectrum of interest was obtained by fitting the experimental data with simulated responses. The CST Microwave Studio and COMSOL models were optimized using the experimental data to provide accurate means of designing the desired metamaterial structures.

Metamaterial films capable of nearly 100% absorptivity around frequency 3.8 THz and 4.75 THz frequencies were designed and successfully fabricated using simple square resonators.

In order to obtain a broad band response on the entire band of a typical LWIR cameras (20 - 40 THz), several configurations were simulated with relatively complex unit cell configurations. These configurations involved combinations of rings and triangular and circular shapes as resonators within the unit cell. Some fabrication and characterization rounds helped to tune the models. The best results were selected to be integrated into the THz-to-IR converter in future work. Also, the possibility to change the fabrication process to obtain stoichiometric Si_3N_4 and further improve the conversion efficiency was investigated.

Some restrictions on the fabrication capabilities have limited the scope of this work. The most impacting one was the non-uniformity of SiN_x films, which has caused photolithography inconsistencies. Furthermore, metamaterials with resonant responses between 5 to 6.5 THz and greater than 40 THz were not obtained even for simple square geometries. Once this gap is filled, the missing data will allow greater accuracy in the finite element models.

Despite the advances of the THz-to-IR development reported in this work, other approaches should be pursued. It may be wise to consider different dielectric materials, especially ones that do not absorb in the LWIR spectral range. This would provide much more flexibility in the spectral shaping of the emissivity on the emitter side. The possibility of using air gaps between resonators and ground planes (mushroom architecture) should also be considered. This would significantly reduce the thermal mass and would make the converter faster and more efficient. Constructing a complete finite element model that includes all phenomena including absorption, emission, heat transfer, and radiative flux transfer would provide a more efficient tool to evaluate the conversion efficiency for each designed configuration.

LIST OF REFERENCES

[1] B. Ferguson, and X. Zhang, "Material for terahertz science and technology," *Natural Materials*, vol. 1, pp. 26-33, Sep. 2002.

[2] R. Knipper, A. Brahm, E. Heinz, T. May, G. Notni, H. Meyer, A. Tünnermann, and J. Popp, "THz Absorption in Fabric and Its Impact on Body Scanning for Security Application," *IEEE Transactions on Terahertz Science and Technology*, vol. 5, no. 6, pp. 999-1004, Nov. 2015.

[3] F. Alves, L. Pimental, D. Grbovic and G. Karunasiri, "MEMs terahertz-to-infrared band converter using frequency selective planar metamaterial," *Scientific Reports*, Aug. 2018.

[4] F. Alves, D. Grbovic, B. Kearney, N. Lavrik and G. Karunasiri, "Bi-material terahertz sensors using metamaterial structures," *Optical Society of America*, vol. 21, no.11, pp. 13256-13271, Jun. 2013.

[5] M. Polyanskiy, "Refractiveindex.info," 2008-2018. [Online]. Available: http://refractiveindex.info. [Accessed 9 Jan 2019].

[6] F. Alves, B. Kearney, D. Grbovic, N. Lavrik and G. Karunasiri, "Strong terahertz absorption using $Si0_2$/Al based metamaterial structures," *Applied Physics Letter* 100, 111104, 2012.

[7] B. Kelechava, "Cleanroom and Controlled Environment Attire," *American National Standards Institute*, 15, Jul. 2015. [Online]. Available: https://blog.ansi.org/2015/07/cleanroom-and-controlled-environment/#gref

[8] L. Pimental, "Metasurface-based MEMS THz-to-IR Focal Plan Array," M.S. thesis, Dept. App Physics, Naval Postgraduate School, Monterey, CA, Sep. 2018.

[9] A. Phillips, "Resonant terahertz absorption using metamaterial structures," M.S. thesis, Dept. Physics, Naval Postgraduate School, Monterey, CA, Dec. 2012.

[10] Computer Simulation Technology, "Workflow and Solver overview," Accessed January 9, 2019. [Online]. Available: https://www.rose-hulman.edu/class/ee/HTML/ECE340/PDFs/MWS_Tutorials.pdf

[11] C. Gong, M. Zhan, J. Yang, Z. Wang, H. Liu, Y. Zhao and W. Liu, "Broadband terahertz metamaterial absorber based on sectional asymmetric structures," *Scientific Reports*, Aug, 2016.

[12] S. Emilie, W. Leo, H. Jean-Paul, B. Mondher, S. Christophe and G. Jean-Jacques, "Enhancing thermal radiation with nanoantennas to create infrared source with high modulation rates," *Optica*, vol. 5, no. 2, pp. 175-179, Feb. 2018.

[13] H. Dang, V. Nguyen, D. Le, H. Nguyen, M. Tran, D. Le and D. Vu, “Broadband metamaterial perfect absorber obtained by coupling effect,” *Journal of Nonlinear Optical Physics & Materials*, vol. 26, no. 3, pp. 1750036, 2017.

INITIAL DISTRIBUTION LIST

1. Defense Technical Information Center
   Ft. Belvoir, Virginia

2. Dudley Knox Library
   Naval Postgraduate School
   Monterey, California